Electronic Supplementary Information

Synthesis, supramolecular aggregation, and NIR-II phosphorescence of isocyanorhodium(I) zwitterions

Wenxuan Wei,[a] Jun Wang,*[b] Xiaomei Kang,[a] Haoquan Li,[a] Qun He,[a] Guanjun Chang [c] and Weifeng Bu *[ad]

[a] Key Laboratory of Nonferrous Metals Chemistry and Resources Utilization of Gansu Province, State Key Laboratory of Applied Organic Chemistry, and College of Chemistry and Chemical Engineering, Lanzhou University, Lanzhou, 730000, China

[b] Hunan Province Cooperative Innovation Center for Molecular Target New Drug Study, School of Pharmaceutical Science, Hengyang Medical School, University of South China, Hengyang, 421001, China

[c] State Key Laboratory of Environment-friendly Energy Materials & School of Material Science and Engineering, Southwest University of Science and Technology, Mianyang, 621010, China

[d] State Key Laboratory of Solid Lubrication, Lanzhou Institute of Chemical Physics, Chinese Academy of Sciences, Lanzhou 730000, China

*Corresponding Author(s): Weifeng Bu: buwf@lzu.edu.cn; Jun Wang: wangjun@usc.edu.cn

1 Experimental Procedures

1.1 Materials

1-Naphthylamine (99%), 2-naphthylamine (98%), 1-amino-2-methylnaphthalene (97%), 4-aminobiphenyl (99%), isocyanobenzene (**L-1**, 98%), 2,6-xylylisocyanide (**L-2**, 97%), and phosphorus(V) oxychloride (99.5%) were purchased from Energy Chemical. Chloro(1,5-cyclooctadiene)rhodium(I) dimer ($[Rh(COD)Cl]_2$, 98%) were purchased from Aladdin Chemical. Formic acid (98%) and triethylamine (99.5%) were purchased from Chron Chemical. Chromatographic or analytical grade solvents, including dimethyl sulfoxide (DMSO), toluene, methanol, and dichloromethane, were commercially available from Tianjin Rionlon Chemical. All these chemicals were directly used without further purification. Water was purified by an Ultrapure Water System model CPW-101 (Advantec, Japan), and its resistance was larger than 18.0 MΩ. 2-Isocyanonaphthalene (**L-3**),[S1] 1-isocyanonaphthalene (**L-4**),[S2] 4-isocyano-1,1′-biphenyl (**L-6**),[S3] and sodium 4-isocyanobenzoate (**L-7**)[S4] were synthesized according to the reported procedures in the related literatures, and they showed identical ^{1}H NMR spectra to those reported therein. 1-Isonitrile-2-methylnaphthalene (**L-5**) was synthesized by a previously reported Ugi procedure[S5] using 1-amino-2-methylnaphthalene as an amino-precursor (Fig. S1−S4).

1.2 Instruments

^{1}H and ^{13}C NMR spectra were recorded on a JNM-ECS400 spectrometer. Deuterated solvents such as $CDCl_3$, CD_3OD, and/or D_2O were employed to dissolve isocyanide ligands and their corresponding rhodium(I) complexes, in which TMS was used as an internal standard. High-resolution electrospray ionization mass spectra (HR-ESI-MS) were obtained on a Bruker APEX II FT-MS mass spectrometer. Fourier transformation infrared (FT-IR) spectra were collected on a Nicolet NEXUS 670 spectrometer using KBr disks. C, H, and N elemental analyses of isocyanorhodium(I) complexes were obtained with Elementar Analysensysteme GmbH VarioEL element analyzer. UV-vis absorption spectra were recorded on Shimadzu 2550/3600i spectrophotometers. Emission spectra, quantum yields (Φ) and lifetimes were measured by using an Edinburgh Instruments FLS1000 fluorescence spectrometer. The quantum yields of the samples were obtained according to an absolute method by utilizing an integrating sphere, during which a 450 W Xe arc lamp was used as the steady state excitation source. Additional luminescence quantum yields (Φ) of isocyanorhodium(I) zwitterions of **1**−**6** in dilute methanol or DMSO solutions (5.0×10^{-5} mol/L) were estimated by using $[Ru(bpy)_3]Cl_2$ (in water, $\Phi = 0.040$) as the reference.[S6,S7] The zeta potentials of zwitterions **1**−**6** at a concentration of 0.1 mmol L^{-1} were obtained on a Malvern Zeta sizer at a fixed detection angle of 173°. Dynamic light scattering (DLS) measurements were performed on a Brookhaven BI-200SM spectrometer. Transmission electron microscopy (TEM) images were obtained from an FEI Tecnai F30 operating at 300 kV. The samples for TEM imaging were prepared by drop-casting dilute solutions onto a carbon-coated copper grid. Wide-angle X-ray scattering (WAXS) experiments were performed on a Nano-inXider (λ = 0.154 nm, Xenocs, France). The X-ray source was a 40 mm-microfocus sealed tube with a copper anode and the total power was 30 W. The concentration of Rh atom in polymer nanoparticles was determined by inductively coupled plasma-mass spectrometry (ICP-MS) (iCAPQc, PerkinElmer).

1.3 Synthesis and Characterization

1-Isonitrile-2-methylnaphthalene (L-5, Scheme S1, Fig. S1−S3). To an oven-dried two-necked flask equipped with a magnetic stirrer and water-cooled condenser, 1-amino-2-methylnaphthalene (1.57 g, 10 mmol), formic acid (1.84 g, 98%, 40 mmol), and toluene (50 mL) were added. The reaction mixture was evacuated and flushed with high-purity argon. This procedure was repeated three times. The reaction mixture was refluxed with stirring for 8 h. After cooling to room temperature, the mixture was evaporated to dryness. The residue was treated with a new portion of toluene (50 mL), which was evaporated again to give the crude product of 1-formamide-2-methylnaphthalene. To a flask with crude 1-formamide-2-methylnaphthalene was added triethylamine (10 mL, 72 mmol) and dichloromethane (50 mL). The resulting solution was cooled to 0 °C (ice-water bath) and phosphorous(V) oxychloride ($POCl_3$, 2.25 ml, 24 mmol) was added dropwise over 30 min. After the addition of $POCl_3$, the mixture was stirred for 1 h at 0 °C (ice-water bath) and 2 h at room temperature. Then, the reaction mixture was poured into ice and neutralized carefully with Na_2CO_3. The organic phase was separated and the aqueous phase was extracted with dichloromethane (3×30 mL). The collected organic phase was washed with brine, and dried over anhydrous sodium sulfate. The mixture was filtered to remove sodium sulfate, and the resulting filtrate was concentrated. The light brown product was purified by flash chromatography (ethyl acetate/petroleum ether = 1:8)**.** Yield: 1.30 g, 78%. ^{1}H NMR (400 MHz, $CDCl_3$, ppm): δ 8.16 (d, J = 8.5 Hz, 1H), 7.85 (d, J = 8.1 Hz, 1H), 7.80 (d, J = 8.5 Hz, 1H), 7.65 (t, J = 7.7 Hz, 1H), 7.54 (t, J = 7.5 Hz, 1H), 7.36 (d, J = 8.5 Hz, 1H), 2.63 (s, 3H). ^{13}C NMR (100 MHz, $CDCl_3$, ppm): δ 169.03, 133.59, 131.98, 129.16, 128.18, 128.05, 127.81, 126.54, 122.73, 19.27. FT-IR (KBr): ν(N≡C) = 2116 cm^{-1}, strong. HR-ESI-MS: m/z calculated for $[C_{12}H_9N+H]^+$: 168.0808. Found: 168.0807. Elemental analysis calculated (%) for $C_{12}H_9N$: C 86.20, H 5.43, N 8.38. Found: C 86.01, H 5.35, N 8.24.

$[Rh(C{\equiv}N\text{-phenyl})_3Cl]$ (RhCl-1, Scheme S2). L-1 (77.3 mg, 0.75 mmol) was added to a solution of $[Rh(COD)Cl]_2$ (61.6 mg, 0.125 mmol) in dichloromethane (5 mL) at room temperature. The mixture was stirred at room temperature

for 30 min, and then 25 mL of hexane was added. The resulting brown precipitate was collected by filtration and washed with hexane and diethyl ether. Yield: 74 mg, 67%. ^{1}H NMR (400 MHz, CD_3OD, ppm): δ 7.41 (broad, 9H), 7.36 (broad, 6H). HR-ESI-MS: m/z calculated for $[C_{21}H_{15}ClN_3Rh-Cl]^+$: 412.0316. Found: 412.0313. FT-IR (KBr): ν(N≡C) = 2137 cm^{-1}, strong. Elemental analysis calculated (%) for $C_{21}H_{15}ClN_3Rh$: C 56.34, H 3.38, N 9.39. Found: C 56.09, H 3.61, N 9.15.

The neutral complexes of **RhCl-2**−**RhCl-6** were synthesized by the similar procedure for **RhCl-1**, but using **L-2**−**L-6** as reacting ligands, respectively.

[Rh(C≡N-2,6-xylyl)$_3$Cl] (RhCl-2). RhCl-2 was synthesized as a yellow solid by utilizing a similar procedure.[S8] Yield: 99 mg, 76%. ^{1}H NMR (400 MHz, $CDCl_3$, ppm): δ 7.22-7.16 (m, 2H), 7.16-7.11 (m, 1H), 7.07 (dd, J_1 = 13.7, J_2 = 7.5 Hz, 6H), 2.49 (s, 12H), 2.39 (s, 6H). HR-ESI-MS: m/z calculated for $[C_{27}H_{27}ClN_3Rh-Cl]^+$: 496.1255. Found: 496.1252. FT-IR (KBr): ν(N≡C) = 2126, 2095 cm^{-1}, strong. Elemental analysis calculated (%) for $C_{27}H_{27}ClN_3Rh$: C 60.97, H 5.12, N 7.90. Found: C 60.51, H 5.54, N 7.79.

[Rh(C≡N-2-naphthyl)$_3$Cl] (RhCl-3). Brown solid. Yield: 130 mg, 92%. ^{1}H NMR (400 MHz, $CDCl_3$, ppm): δ 8.04 (d, J = 9.0 Hz, 2H), 8.04 (d, J = 9.0 Hz, 2H), 7.93-7.79 (m, 11H), 7.61-7.52 (m, 8H). HR-ESI-MS: m/z calculated for $[C_{33}H_{21}ClN_3Rh-Cl]^+$: 562.0785; Found: 562.0782. FT-IR (KBr): ν(N≡C) = 2152 cm^{-1}, strong. Elemental analysis calculated (%) for $C_{33}H_{21}ClN_3Rh$: C 66.29, H 3.54, N 7.03. Found: C 66.63, H 3.19, N 7.14.

[Rh(C≡N-1-naphthyl)$_3$Cl] (RhCl-4). Dark green solid. Yield: 110 mg, 74%. ^{1}H NMR (400 MHz, $CDCl_3$, ppm): δ 8.49-8.39 (m, 2H), 8.30 (d, J = 8.4 Hz, 1H), 7.96-7.86 (m, 6H), 7.72 (d, J = 7.3 Hz, 2H), 7.61-7.52 (m, 6H), 7.49-7.42 (m, 4H). HR-ESI-MS: m/z calculated for $[C_{33}H_{21}ClN_3Rh-Cl]^+$: 562.0785; Found: 562.0776. FT-IR (KBr): ν(N≡C) = 2119 cm^{-1}, strong. Elemental analysis calculated (%) for $C_{33}H_{21}ClN_3Rh$: C 66.29, H 3.54, N 7.03. Found: C 66.05, H 3.42, N 7.08.

[Rh(C≡N-2-methylnaphthyl)$_3$Cl] (RhCl-5). Purple solid. Yield: 110 mg, 69%. ^{1}H NMR (400 MHz, $CDCl_3$, ppm): δ 8.49-8.39 (m, 2H), 8.30 (d, J = 8.4 Hz, 1H), 7.97-7.86 (m, 6H), 7.72 (d, J = 7.3 Hz, 2H), 7.62-7.52 (m, 6H), 7.50-7.41 (m, 4H). HR-ESI-MS: m/z calculated for $[C_{36}H_{27}ClN_3Rh-Cl]^+$: 604.1255. Found: 604.1251. FT-IR (KBr): ν(N≡C) = 2119, 2073 cm^{-1}, strong. Elemental analysis calculated (%) for $C_{36}H_{27}ClN_3Rh$: C 67.56, H 4.25, N, 6.57. Found: C 67.11, H 4.33, N 6.69.

[Rh(C≡N-4-biphenyl)$_3$Cl] (RhCl-6). Brown solid. Yield: 150 mg, 90%. ^{1}H NMR (400 MHz, $CDCl_3$, ppm): δ 7.65-7.60 (m, 4H), 7.56 (m, 10H), 7.50-7.42 (m, 8H), 7.42-7.36 (m, 5H). HR-ESI-MS: m/z calculated for $[C_{39}H_{27}ClN_3Rh-Cl]^+$: 640.1255. Found: 640.1243. FT-IR (KBr): ν(N≡C) = 2158 cm^{-1}, strong. Elemental analysis calculated (%) for $C_{39}H_{27}ClN_3Rh$: C 66.29, H 3.54, N 7.03. Found: C 66.70, H 3.81, N 7.26.

[Rh(C≡N-2,6-xylyl)$_3$(C≡N-4-benzoate)] (2). RhCl-2 (26.6 mg, 0.05 mmol) was dissolved in dichloromethane (3 mL), and to this was added sodium 4-isocyanobenzoate (**L-7**, 8.87 mg, 0.0525 mmol) in methanol (3 mL). The mixture was stirred at room temperature for 30 min. The crude sample was collected by evaporating the solvents under reduced pressure, which was further dissolved in 2 mL of methanol. The resulting solution was placed in a dialysis bag (MWCO, 1 kDa) and dialyzed against distilled water for 24 h. The pure zwitterion of **2** was obtained as a dark green solid by freeze-drying. Yield: 29 mg, 89%. ^{1}H NMR (400 MHz, CD_3OD, ppm): δ 8.06 (d, J = 8.3 Hz, 2H), 7.62 (d, J = 8.2 Hz, 2H), 7.42-7.32 (m, 3H), 7.26 (d, J = 7.6 Hz, 6H), 2.49 (s, 18H). HR-ESI-MS: m/z calculated for $[C_{35}H_{31}N_4O_2Rh+H]^+$: 643.1575. Found: 643.1566. FT-IR (KBr): ν(N≡C) = 2144 cm^{-1}, strong; ν(COO^-) = 1563 cm^{-1}, strong. Elemental analysis calculated (%) for $C_{35}H_{31}N_4O_2Rh$: C 65.42, H 4.86, N 8.72. Found: C 65.75, H 4.55, N 8.91.

The zwitterionic complexes of **1** and **3**−**6** were synthesized by the similar procedure for **2**, but using **RhCl-1** and **RhCl-3**−**RhCl-6** as reacting precursors, respectively.

[Rh(C≡N-phenyl)$_3$(C≡N-4-benzoate)] (1). Dark green solid. Yield: 28 mg, 87%. ^{1}H NMR (400 MHz, CD_3OD, ppm): δ 8.08 (d, J = 8.5 Hz, 8H), 7.65 (d, J = 8.5 Hz, 9H), 7.56 (d, J = 5.7 Hz, 2H). HR-ESI-MS: m/z calculated for $[C_{29}H_{19}N_4O_2Rh+H]^+$: 559.0636. Found: 559.0630. FT-IR (KBr): ν(N≡C) = 2151 cm^{-1}, strong; ν(COO^-) = 1565 cm^{-1}, strong. Elemental analysis calculated (%) for $C_{29}H_{19}N_4O_2Rh$: C 62.38, H 3.43, N 10.03. Found: C 62.61, H 3.32, N 9.97.

[Rh(C≡N-2-naphthyl)$_3$(C≡N-4-benzoate)] (3). Black solid. Yield: 28 mg, 80%. ^{1}H NMR (400 MHz, CD_3OD, ppm): δ 8.26 (s, 2H), 8.07 (d, J = 7.7 Hz, 7H), 8.03 (d, J = 9.1 Hz, 2H), 7.96 (d, J = 7.2 Hz, 3H), 7.65 (dd, J_1 = 14.2, J_2 = 6.0 Hz, 11H). HR-ESI-MS: m/z calculated for $[C_{41}H_{25}N_4O_2Rh+H]^+$: 709.1105; Found: 709.1111. FT-IR (KBr): ν(N≡C) = 2148 cm^{-1}, strong; ν(COO^-) = 1557 cm^{-1}, strong. Elemental analysis calculated (%) for $C_{41}H_{25}N_4O_2Rh$: C 69.50, H 3.56, N 7.91. Found: C 69.04, H 3.71, N 7.63.

[Rh(C≡N-1-naphthyl)$_3$(C≡N-4-benzoate)] (4). Dark green solid. Yield: 27 mg, 76%. ^{1}H NMR (400 MHz, CD_3OD, ppm): δ 7.64 (t, J = 8.3 Hz, 6H), 7.52 (dd, J_1 = 13.7, J_2 = 8.2 Hz, 5H), 7.30 (t, J = 7.2 Hz, 3H), 7.14–6.88 (m, 9H), 6.80 (d, J = 7.5 Hz, 2H). HR-ESI-MS: m/z calculated for $[C_{41}H_{25}N_4O_2Rh+H]^+$: 709.1105. Found: 709.1107. FT-IR (KBr): ν(N≡C) = 2145 cm^{-1}, strong; ν(COO^-) = 1559 cm^{-1}, strong. Elemental analysis calculated (%) for $C_{41}H_{25}N_4O_2Rh$:·C

69.50, H 3.56, N 7.91. Found: C 69.21, H 3.89, N 7.56.

[Rh(C≡N-2-methylnaphthyl)$_3$(C≡N-4-benzoate)] (5). Green solid. Yield: 34 mg, 90%. ^{1}H NMR (400 MHz, CD_3OD, ppm): δ 7.95-7.66 (m, 11H), 7.44 (t, J = 7.3 Hz, 3H), 7.33-7.07 (m, 8H), 2.49 (s, 9H). HR-ESI-MS: m/z calculated for $[C_{44}H_{31}N_4O_2Rh+H]^+$: 751.1575. Found: 751.1573. FT-IR (KBr): ν(N≡C) = 2141 cm^{-1}, strong; ν(COO^-) = 1558 cm^{-1}, strong. Elemental analysis calculated (%) for $C_{44}H_{31}N_4O_2Rh$: C 70.40, H 4.16, N 7.46. Found: C 70.59, H 4.02, N 7.27.

[Rh(C≡N-4-biphenyl)$_3$(C≡N-4-benzoate)] (6). Black solid. Yield: 28 mg, 71%. ^{1}H NMR (400 MHz, CD_3OD, ppm): δ 8.08 (d, J = 8.5 Hz, 8H), 7.78 (m, 6H), 7.68 (d, J = 8.4 Hz, 11H), 7.45 (m, 6H). HR-ESI-MS: m/z calculated for $[C_{47}H_{31}N_4O_2Rh+H]^+$: 787.1575. Found: 787.1578. FT-IR (KBr): ν(N≡C) = 2144 cm^{-1}, strong; ν(COO^-) = 1534 cm^{-1}, strong. Elemental analysis calculated (%) for $C_{47}H_{31}N_4O_2Rh$: C 71.76, H 3.97, N 7.12. Found: C 71.33, H 3.90, N 7.46.

1.4 Concentration-Dependent UV-vis Absorption Spectroscopic Studies

The low-energy absorption bands that appear with increasing the concentration can be explicated by the oligomerization of the zwitterionic rhodium(I) complexes:[S9–S12]

$$2\mathrm{M} \overset{\mathrm{K1}}{\leftrightarrow} \mathrm{D} \quad (1)$$

$$\mathrm{D} + \mathrm{M} \overset{\mathrm{K2}}{\leftrightarrow} \mathrm{T} \quad (2)$$

The equations (1) represents the monomer-dimer equilibria and (2) is the dimer-trimer equilibria, where M, D, and T are monomer, dimer, and trimer species, respectively. In the analysis of these equilibria, equations (1) and (2) have been used to give mathematical expressions for (3) and (4):

$$\frac{[\mathrm{Rh}]}{\mathrm{A}_2^{1/2}} = \frac{1}{(\varepsilon_2\mathrm{K}_1)^{1/2}} + \frac{2\mathrm{A}_2^{1/2}}{\varepsilon_2} + \frac{3\mathrm{K}_2\mathrm{A}^2}{\varepsilon_2(\varepsilon_2\mathrm{K}_1)^{1/2}} \quad (3)$$

$$\mathrm{A}_3 = \frac{\varepsilon_3\mathrm{K}_2\mathrm{A}_2^{3/2}}{\varepsilon_2(\varepsilon_2\mathrm{K}_1)^{1/2}} \quad (4)$$

where [Rh] is the total concentration of the zwitterionic rhodium(I) complexes in terms of monomer species, A_2 and A_3 are the absorbances due only to dimers and trimers, respectively, and ε_2 and ε_3 are the corresponding molar extinction coefficients. The corresponding dimerization constant K_1 was obtained from the slope ($2/\varepsilon_2$) and intercept ($1/(\varepsilon_2K_1)^{1/2}$ by plotting $[Rh]/A_2^{1/2}$ vs A_2 as a straight line in equation (3). Similarly, the trimerization constant K_2 can be determined by plotting A_3 vs $A_2^{3/2}$ (equation (4)) as a straight line with the slope $\varepsilon_3K_2/\varepsilon_2(\varepsilon_2K_1)^{1/2}$ (ε_3 can be estimated as $1.5\varepsilon_2$).

1.5 Temperature-Dependent Isodesmic Self-Assembly Model

For an isodesmic mechanism, assuming a two-state equilibrium, the degree of aggregation or the molar fraction of aggregated species $\alpha_{agg}(T)$ can be related to temperature by means of a sigmoidal relation.[S10–S14] This can be rationalized by taking into account that still up to a high degree of aggregation $\alpha_{agg}(T)$, only short oligomers are present. Under this assumption, equation 5 expresses the normalized degree of aggregation $\alpha_{agg}(T)$ as a function of the temperature T, with values between 0 and 1 at different temperatures, being given by:

$$\alpha_{agg}(T) = \frac{1}{1+[-0.908\Delta H\frac{T-Tm}{RTm^2}} \quad (5)$$

The temperature for α = 0.5 is defined the melting temperature T_m, and R is the ideal gas constant. The enthalpy change (ΔH) of the aggregation process can therefore be deduced upon fitting the normalized degree of aggregation as a function of temperature.

1.6 Calculations of the Dimerization Constant and Curve-Fitting by Using NMR Dimerization Model in the Concentration-Dependent Self-Associating System

In a monomer-dimer equilibrium system, where there is a rapid interconversion that two monomers A would associate to form a dimer A_2, as represented in equation (6):[S10–S12,S15–S17]

$$\mathrm{A} + \mathrm{A} \rightleftharpoons \mathrm{A}_2 \quad (6)$$

Determination of the dimerization constant K for the self-association process can be expressed as:

$$\mathrm{K} = \frac{[\mathrm{A}_2]}{[\mathrm{A}]^2} \quad (7)$$

$$[\mathrm{A}_0] = [\mathrm{A}] + 2[\mathrm{A}_2] \quad (8)$$

Where [A], [A_2], and [A_0] are monomer, dimer, and total concentration of complexes, respectively. It is assumed that the observed chemical shift δ_{obs} is the weighted average of those of the intrinsic chemical shifts of monomer (δ_m) and dimer (δ_d), and δ_{obs} was given by:

$$\delta_{obs} = \delta_d - (\delta_d - \delta_m)\frac{[A]}{[A]_0} \quad (9)$$

Combining equation (7) and (8) gives the equation (10)

$$2K[A]^2 + [A] - [A_0] = 0 \quad (10)$$

Solving for [A] in equation (10) gives:

$$[A] = \{(1 + 8K[A_0])^{1/2} - 1\}/4K \quad (11)$$

Consequently, combining equation (9) and (11) gives:

$$\delta_{obs} = \delta_d - (\delta_d - \delta_m)\{(1 + 8K[A_0])^{1/2} - 1\}/4K[A_0] \quad (12)$$

Finally, the three variable parameters K, δ_d, and δ_m can be determined by a nonlinear least-square fit.

1.7 Determination of Distances between Protons by ^{1}H-^{1}H NOESY Spectroscopy

For the ^{1}H-^{1}H NOESY spectra of complexes in CD_3OD or a mixed CD_3OD/D_2O system, the integrals of the cross peaks in the NOESY spectra were extracted. Then the distance (r_1) between H_i and H_h on the benzene ring of 4-isocyanobenzoate (**L-7**) is assumed to be 2.49 Å based on the optimized structure, which was used as a standard.

Using the relation,[S18]

$$\frac{A_1}{A_2} = \frac{{r_2}^6}{{r_1}^6} \quad (13)$$

the distances (r_2) between the protons on **L-2** and **L-5** and **L-7** in zwitterions **2** and **5** can be calculated. In equation 15, A_1 is the integral of cross peaks H_i and H_h, and their value are set to 1, while A_2 is is the integral extracted from NOE signals featuring through-space correlation.

1.8 Curve-Fitting for Solvent-Dependent Self-Assembly

To fit the supramolecular aggregation equilibrium model to the denaturation data acquired on zwitterions **2** and **5**, the normalized degree of aggregation (α_{agg}) is deduced from the changes observed in UV-vis absorption band maxima upon increasing the volume fraction (f) of good solvents, according to equation (14):[S10–S12,S19,S20]

$$\alpha_{agg} = \frac{A(f) - A(f=0)}{A(f=1) - A(f=0)} \quad (14)$$

Where $A(f)$ is the absorbance at a given volume fraction of good solvents.

The cooperativity factor σ is given by equation (15):

$$\sigma = \frac{K_n}{K_e} \quad (15)$$

Where K_n and K_e are the binding constants for the nucleation and elongation steps, respectively. Notably, for the cooperative model $K_n < K_e$ and for isodesmic process $K_n = K_e$ (σ = 1).

The Gibbs free energy gain upon monomer addition is linearly correlated with the good solvent volume fraction f, as described by equation (16) and (17) :

$$K_e = \exp(-\frac{\Delta G^0}{RT}) \quad (16)$$

$$\Delta G^{0\prime} = \Delta G^0 + mf \quad (17)$$

where ΔG^0 represents Gibbs free energy of monomer association, m is the parameter showing the dependence of $\Delta G^{0\prime}$ on f, R is the gas constant, and T is the temperature.

Meijer and coworkers have reported the supramolecular polymerization equilibrium model for solvent-dependent self-assembly.[S19] The denaturation model is described by using the concentration-dependent supramolecular polymerization equilibrium model by Goldstein & Stryer.[S21]

$$\begin{aligned}
X + X &\overset{K_n}{\Leftrightarrow} P_2 \quad & [P_2] &= K_n[X]^2 \\
P_2 + X &\overset{K_n}{\Leftrightarrow} P_3 \quad & [P_3] &= K_n[P_2][X] \\
&\vdots & & \\
P_{n-1} + X &\overset{K_n}{\Leftrightarrow} P_n \quad & [P_n] &= K_n[P_{n-1}][X] \\
P_n + X &\overset{K_e}{\Leftrightarrow} P_{n+1} \quad & [P_{n+1}] &= K_e[P_n][X] \\
&\vdots & &
\end{aligned} \quad (18)$$

$$P_{i-1} + X \overset{K_e}{\Leftrightarrow} P_i \qquad [P_i] = K_e[P_{i-1}][X]$$

The concentration of each species P_i was given by $[P_i] = K_n^{i-1}$ for $i \leq n$, and $[P_i] = K_e^{i-n}K_n^{n-1}[X]^i$ for $i > n$. The dimensionless concentration $p_i = K_e[P_i]$, the dimensionless monomer concentration $x = K_e[X]$, and for dimensionless the concentration of each species P_i: $p_i = \sigma^{i-1} x^i$ ($i \leq n$) and $p_i = \sigma^{n-1}x^i$ ($i > n$). The dimensionless mass balance is obtained:

$$x_{tot} = \sigma^{-1}\sum_{i=1}^{n} i(\sigma x)^i + \sigma^{n-i}\sum_{i=n+1}^{\infty} ix^i \qquad (19)$$

with dimensionless total concentration $x_{tot} = K_e c_{tot}$ and c_{tot}: the total monomer concentration.

Via $K_e = \exp(\frac{-\Delta G_0'}{RT})$, the another expression of x_{tot} was given by :

$$x_{tot} = c_{tot} e^{-(\frac{\Delta G_0 - mf}{RT})} \qquad (20)$$

Evaluating both sums in equation (19) by using standard expressions for converging series yields:

$$x_{tot} = \sigma^{-1}\left(\frac{(\sigma x)^{n+1}(n\sigma x - n - 1)}{(\sigma x - 1)^2} + \frac{\sigma x}{(\sigma x - 1)^2}\right) - \sigma^{n-1}\left(\frac{x^{n+1}(nx - n - 1)}{(x-1)^2}\right) \qquad (21)$$

Solving the sum equation (21) by using standard numerical methods (Matlab *fzero* solver) yields the dimensionless monomer concentration x, i.e.

$$x = F'(x_{\mathrm{tot}}, \sigma) \qquad (22)$$

Defining the species with $i > 1$ as aggregates, the degree of aggregation α_{agg} can be obtained:

$$\alpha_{\mathrm{agg}} = \frac{x_{tot} - x}{x_{tot}} \qquad (23)$$

Combining equation (20), (22) and (23), a function expression (24) of α_{agg} was given:

$$\alpha_{\mathrm{agg}} = F(f, \Delta G_0, m, \sigma\ ) \qquad (24)$$

The optimized parameters (ΔG_0, m, σ) curve-fittings were performed via a non-linear least squares analysis where the sum of the squared residuals is minimized using Matlab (*lsqnonlin* solver). Then the data are fitted with non-linear least squared regression, using the Levenberg-Marquardt algorithm.

1.9 General Procedure for the Synthesis of Polymer Nanoparticles 2-PN and 5-PN

The zwitterion of **2** or **5** (1 mg) and DSPE-mPEG2000 (10 mg) were dissolved in chloroform/methanol = 3:1 (v/v). Then, organic solvents were removed under reduced pressure by a rotary evaporator. Milli-Q water (1 mL) was added to the mixture under sonication for 15 min. The water solution was filtered through a membrane filter (d = 0.22 μm) and adjusted to a suitable concentration with PBS buffer (pH = 7.4) for further use. The obtained clear solutions of **2-PN** and **5-PN** were stored in 4 °C for further usage. In addition, the concentration of Rh atom in polymer nanoparticles was determined by ICP-MS analysis after the polymer nanoparticle were digested with aqua regia.

1.10 Cell Viability Assay

Cancer cell lines (MCF-7, HepG2, Hep3B, and Bel-7404) and normal L02 cells were seeded in 96-well plates (6−8 × 10^3 cells/well) and incubated with DMEM (10% fetal bovine serum and 5% CO_2 at 37 °C). Then the cells in wells were treated with PBS, **2-PN**, and **5-PN**, with three wells for each condition. Thereafter, the cellular viability was assessed via an MTT colorimetric assay. The MTT assay for the above cell lines was performed 24 h and 48 h after drug exposure, respectively. In brief, MTT reagent (10 μL of a 5 mg/mL solution in PBS buffer) was added to each well and the plates were incubated for another 4 h. Acidified SDS solution was then added (100 μL/well) and the plates were kept in the dark for an additional 12 h. Measurements of absorbance were subsequently completed with a microplate reader at 570 nm.

1.11 Dose Dependent Toxicity

To evaluate the biosafety of **2-PN** and **5-PN** in vivo, the dose-dependent toxicity was performed through tail intravenous injection with different doses of **2-PN** and **5-PN** in a mice model. Thirty Balb/c mice were randomly divided into six groups. The control group was treated with PBS and the other five groups were treated with 2.5, 5.0, 10.0, 20.0, and 40.0 mg/kg of **2-PN** and **5-PN** via tail intravenous injection, respectively. The volume of each injection was 100 μL.

1.12 In vivo biosafety studies

To prove the systemic toxicity, the healthy mice were randomly assigned into three groups (3 mice/group), and each mice was intravenously injected with PBS, **2-PN** or **5-PN** (10 mg/kg body weight), respectively. This dosage was consistent with the in vivo fluorescence imaging study. Then the mice were sacrificed after 72 hours of nanoparticles

injection, and the blood samples were collected from the mice eye socket vein for blood chemistry analyses including red/white blood cell counts and hepatic/renal function.

1.13 Tumor Model

All experimental designs and protocols involving animals were approved by the Experimental Animal Ethics Committee of the University of South China, Hunan, People's Republic of China (approval 4304079008946) and complied with the National Institutes of Health and University of South China guidelines on the care and use of animals for scientific purposes. For the construction of tumor-bearing mice, 100 μL of PBS with 5×10^6 Bel-7404 cells was subcutaneously (s.c.) injected into the Balb/c nude mice (female, 4-6 weeks, 16-18 g). The tumor volume was calculated using the following formula: (length × width^2 × 1/2). When the tumor volumes of the mice reached approximately 100 mm^3, the Bel-7404 tumor xenograft model was established.

1.14 In Vivo Biodistribution Imaging

When tumors reached approximately 300 mm^3, **2-PN** and **5-PN** (10 mg/kg body weight) were *i.v.* injected into the mice. *In vivo* fluorescence imaging was carried out with the *In vivo* imaging system at various time points. Mice were sacrificed after 72 hours of nanoparticles injection. *Ex vivo* imaging of organs including heart, liver, spleen, lung, kidney, and tumor.

1.15 H&E Staining Assays

After the tumor size up to about 100 mm^3, the mice were randomly divided into three groups with 5 mice per group. The mice were injected with PBS, **2-PN** and **5-PN** at a dose of 10 mg/kg via tail vein at days 0, 2, 4, 6, 8, 10 and 14. The body weight and tumor volume were measured every 2 days. After the treatment, all mice were sacrificed, and primary organs and tumors were collected for further TUNEL apoptosis and H&E staining assays.

2 Results and Discussion

2.1 Results and Discussion

2.1.1 Synthesis and Characterization

The neutral isocyanorhodium(I) complexes were fully characterized by their ^{1}H NMR spectra, HR-ESI-MS, FT-IR spectra, and elemental analyses. All of the proton resonances were clearly assignable in the ^{1}H NMR spectra (Fig. S4−S9). The HR-ESI-MS of **RhCl-1**−**RhCl-6** exhibited typical peaks of the cationic species (m/z = $[M - Cl]^+$), indicative of the substitutable chloride ligands therein (Fig. S10−S15). FT-IR bands of **RhCl-5** at 2119 and 2073 cm^{-1} were assigned to −N≡C antisymmetric stretching modes, which were red-shifted to 2141 cm^{-1} in zwitterion **5** as a result of highly polar microenvironments of the −N≡C groups (Fig. S22). Moreover, the characteristic band of $-COO^-$ appeared at 1558 cm^{-1}. Similar characteristic FT-IR bands were also observed in the FT-IR spectra of other neutral complexes and zwitterions (Fig. S22).

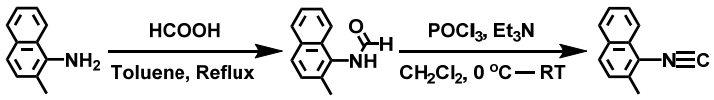

Scheme S1 Synthetic routes of **L-5**.

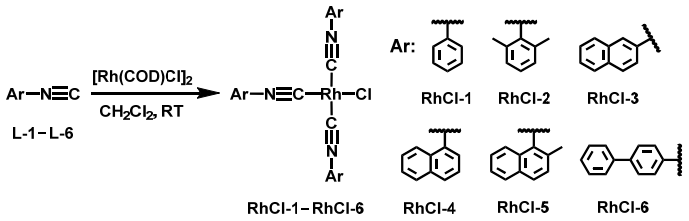

Scheme S2 Synthetic routes of **RhCl-1**−**RhCl-6.**

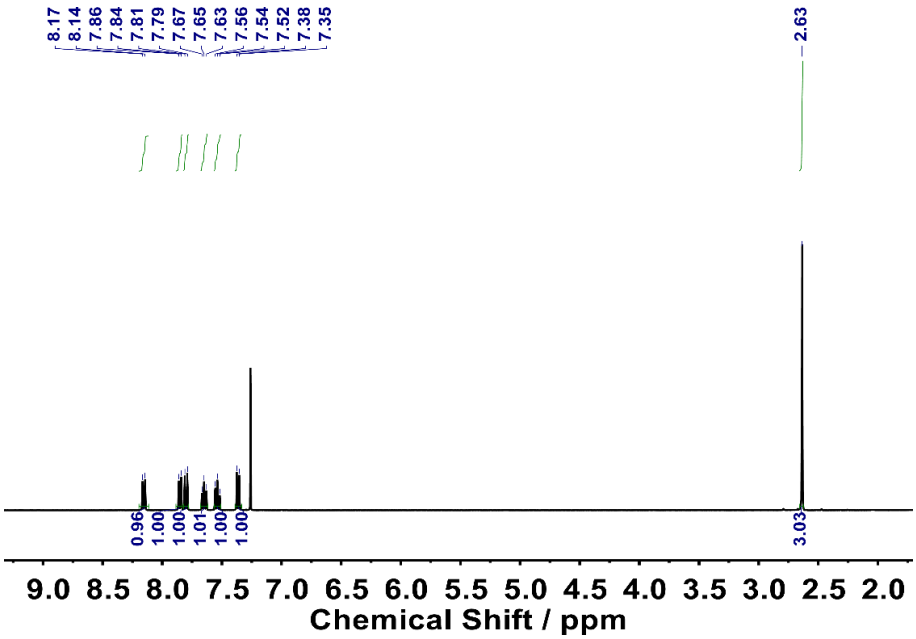

Fig. S1 ^{1}H NMR spectra of **L-5** in $CDCl_3$.

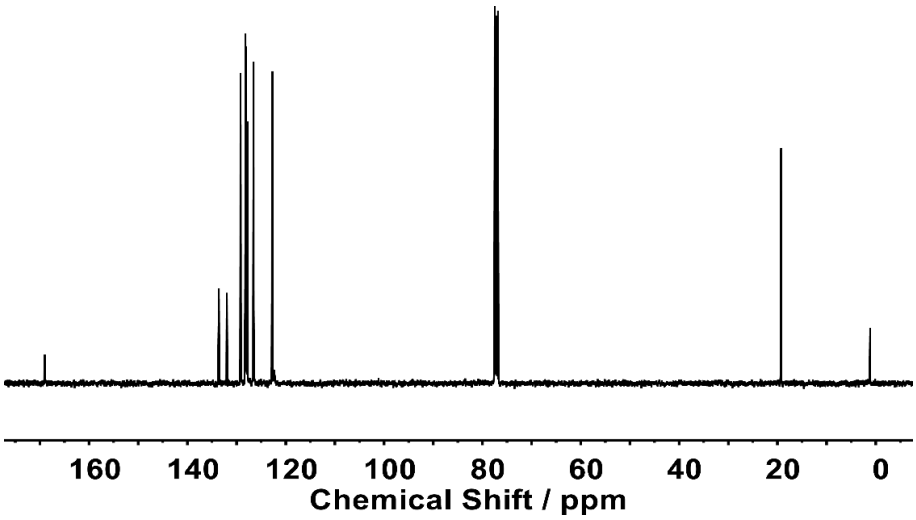

Fig. S2 ^{13}C NMR spectra of **L-5** in $CDCl_3$.

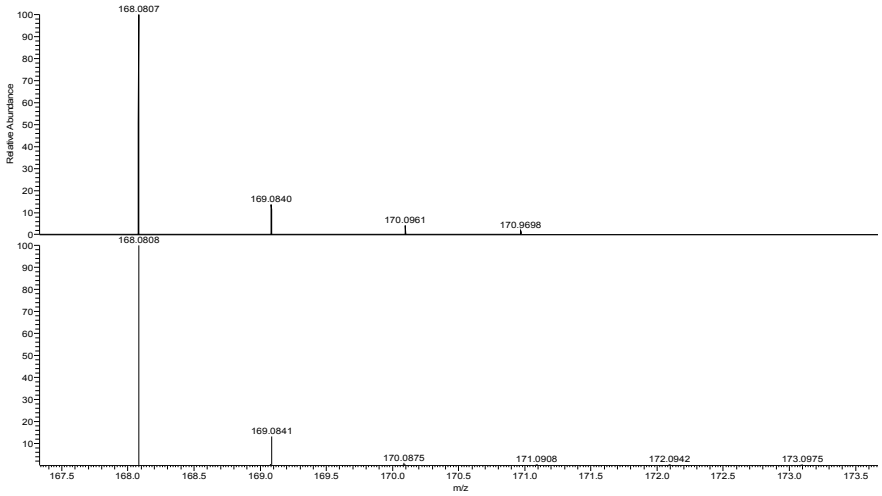

Fig. S3 High-resolution ESI mass spectrum of **L-5**: Experimental (top) and theoretical (bottom) isotope patterns of $[C_{12}H_9N+H]^+$.

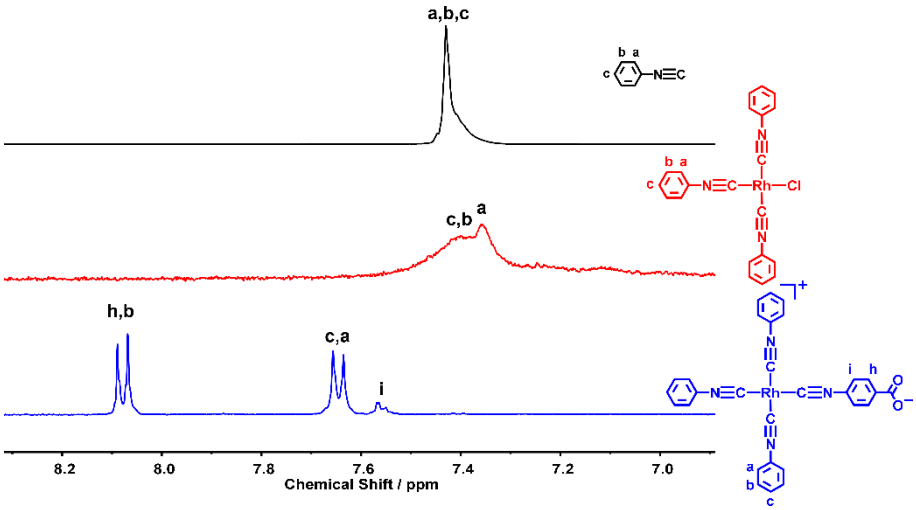

Fig. S4 ^1H NMR spectra of **L-1** (Top, in CD_3OD), **RhCl-1** (Center, in CD_2Cl_2), and **1** (Bottom, in CD_3OD).

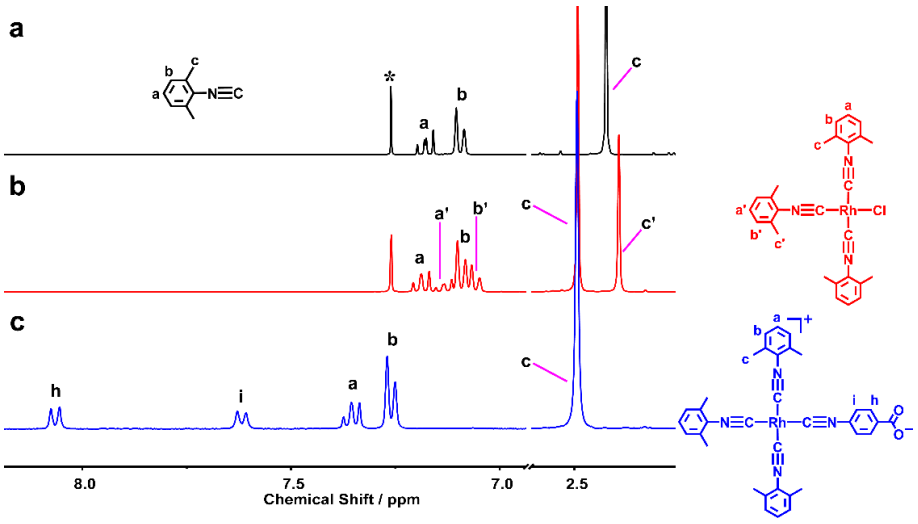

Fig. S5 ^{1}H NMR spectra of **L-2** (Top, in $CDCl_3$), **RhCl-2** (Center, in $CDCl_3$), and **2** (Bottom, in CD_3OD).

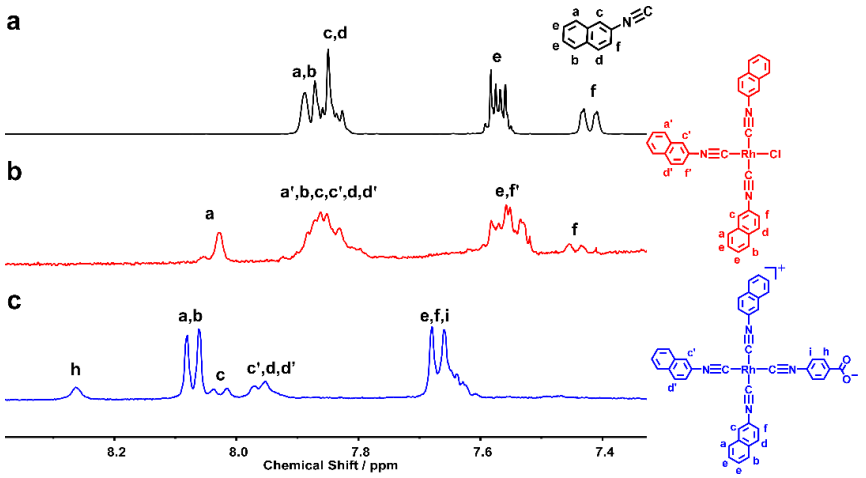

Fig. S6 ^{1}H NMR spectra of **L-3** (Top, in $CDCl_3$), **RhCl-3** (Center, in $CDCl_3$), and **3** (Bottom, in CD_3OD).

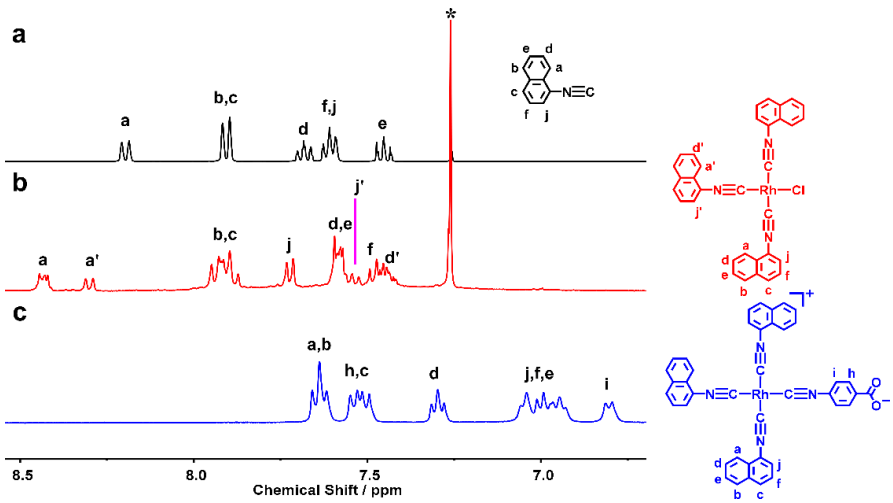

Fig. S7 ^{1}H NMR spectra of **L-4** (Top, in $CDCl_3$), **RhCl-4** (Center, in $CDCl_3$), and **4** (Bottom, in CD_3OD).

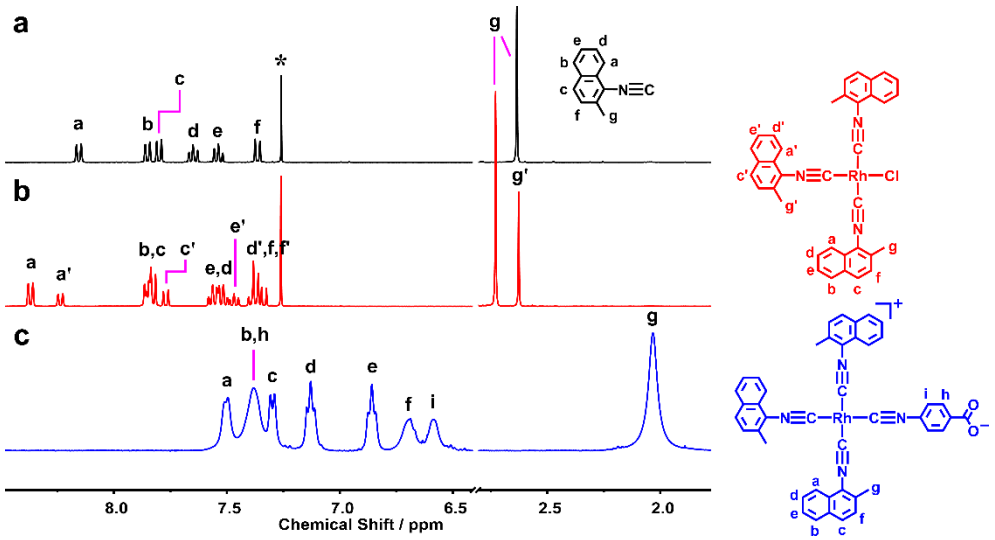

Fig. S8 ^{1}H NMR spectra of **L-5** (Top, in $CDCl_3$), **RhCl-5** (Center, in $CDCl_3$), and **5** (Bottom, in CD_3OD).

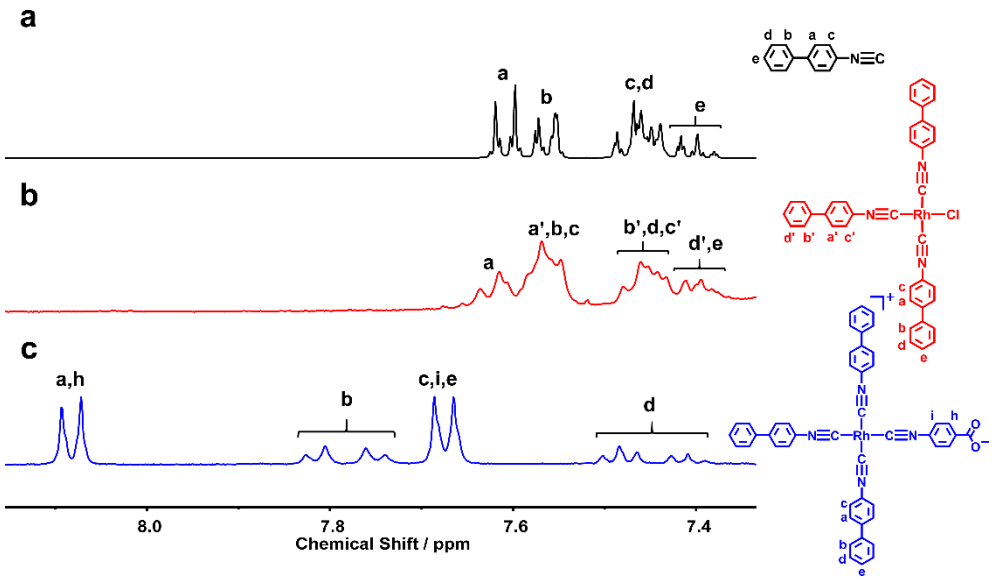

Fig. S9 ^{1}H NMR spectra of **L-6** (Top, in $CDCl_3$), **RhCl-6** (Center, in $CDCl_3$), and **6** (Bottom, in CD_3OD).

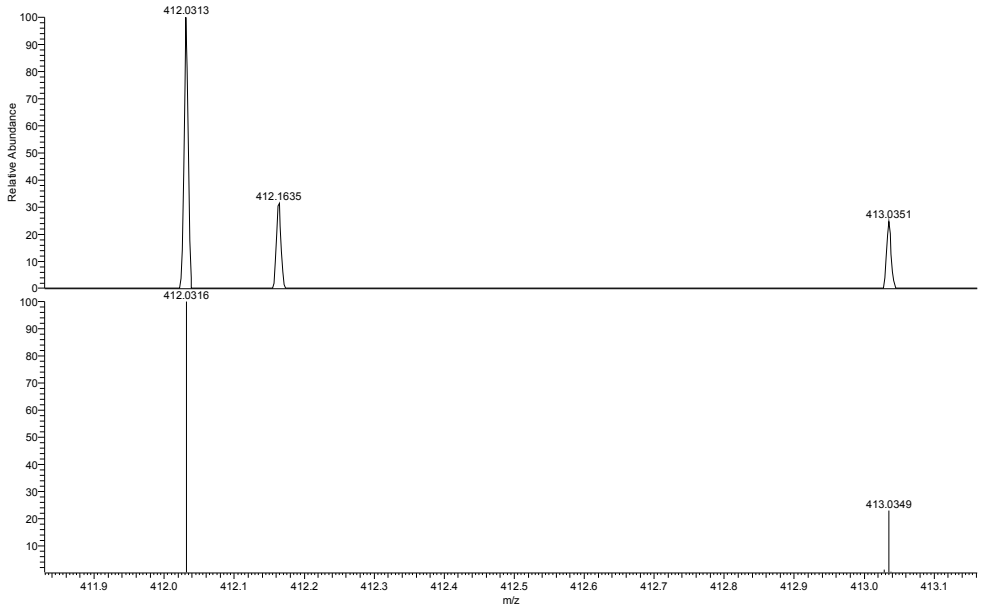

Fig. S10 High-resolution ESI mass spectrum of **RhCl-1**: Experimental (top) and theoretical (bottom) isotope patterns of $[C_{21}H_{15}ClN_3Rh{-}Cl]^+$.

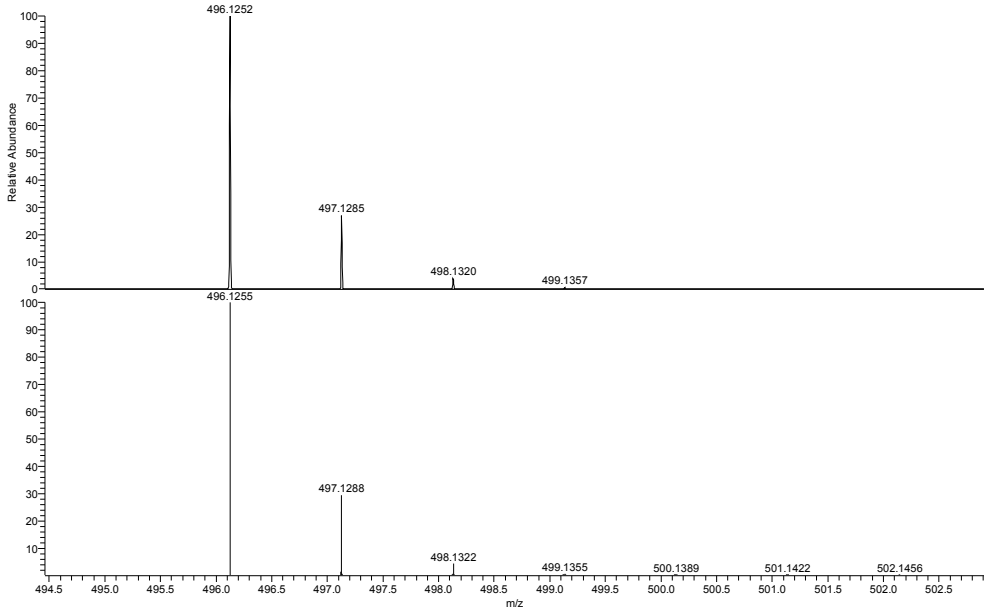

Fig. S11 High-resolution ESI mass spectrum of **RhCl-2**: Experimental (top) and theoretical (bottom) isotope patterns of $[C_{27}H_{27}ClN_3Rh{-}Cl]^+$.

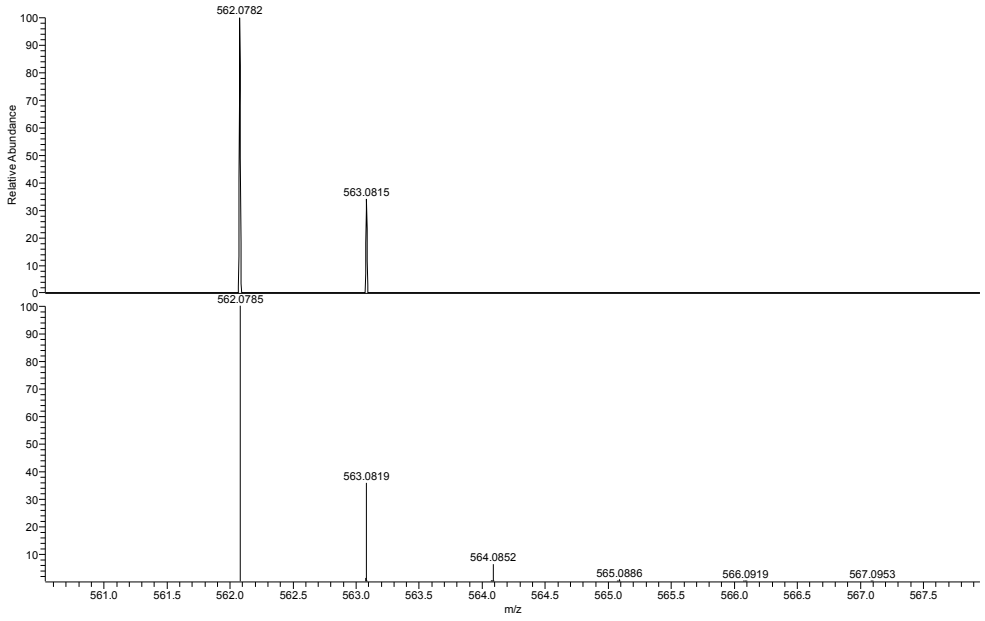

Fig. S12 High-resolution ESI mass spectrum of **RhCl-3**: Experimental (top) and theoretical (bottom) isotope patterns of $[C_{33}H_{21}ClN_3Rh{-}Cl]^+$.

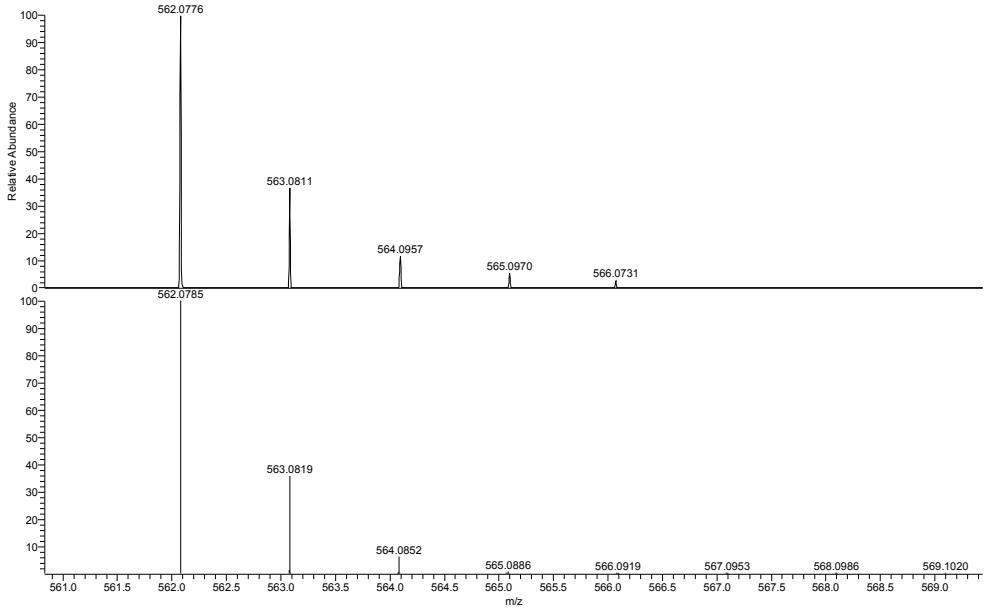

Fig. S13 High-resolution ESI mass spectrum of **RhCl-4**: Experimental (top) and theoretical (bottom) isotope patterns of $[C_{33}H_{21}ClN_3Rh{-}Cl]^+$.

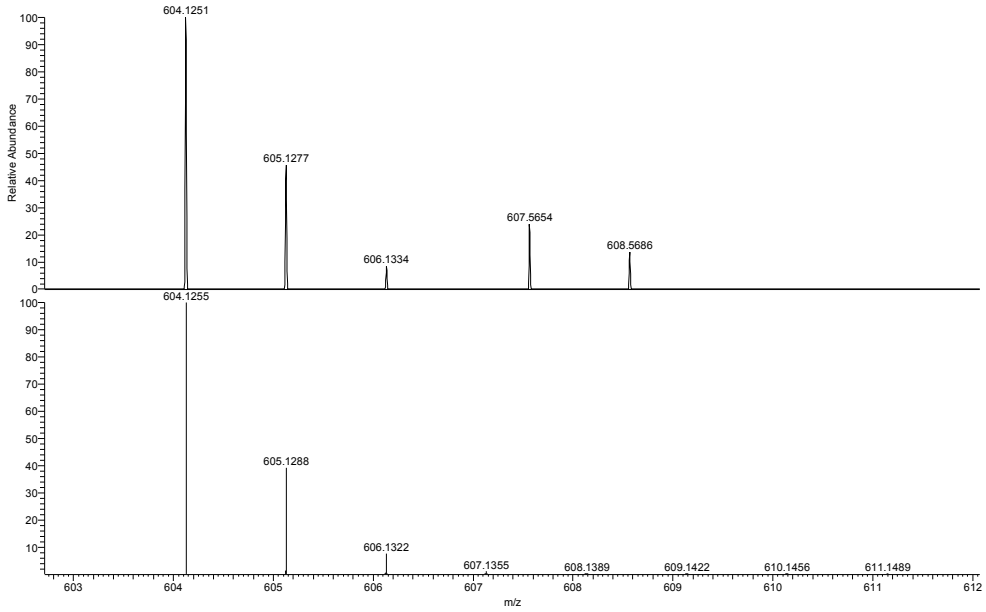

Fig. S14 High-resolution ESI mass spectrum of **RhCl-5**: Experimental (top) and theoretical (bottom) isotope patterns of $[C_{36}H_{27}ClN_3Rh{-}Cl]^+$.

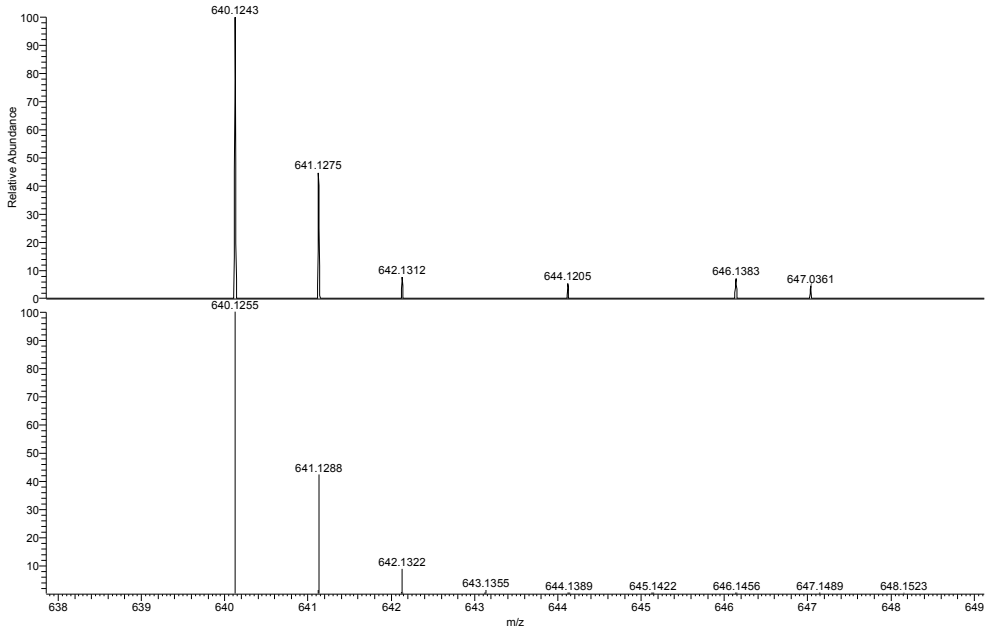

Fig. S15 High-resolution ESI mass spectrum of **RhCl-6**: Experimental (top) and theoretical (bottom) isotope patterns of $[C_{39}H_{27}ClN_3Rh{-}Cl]^+$.

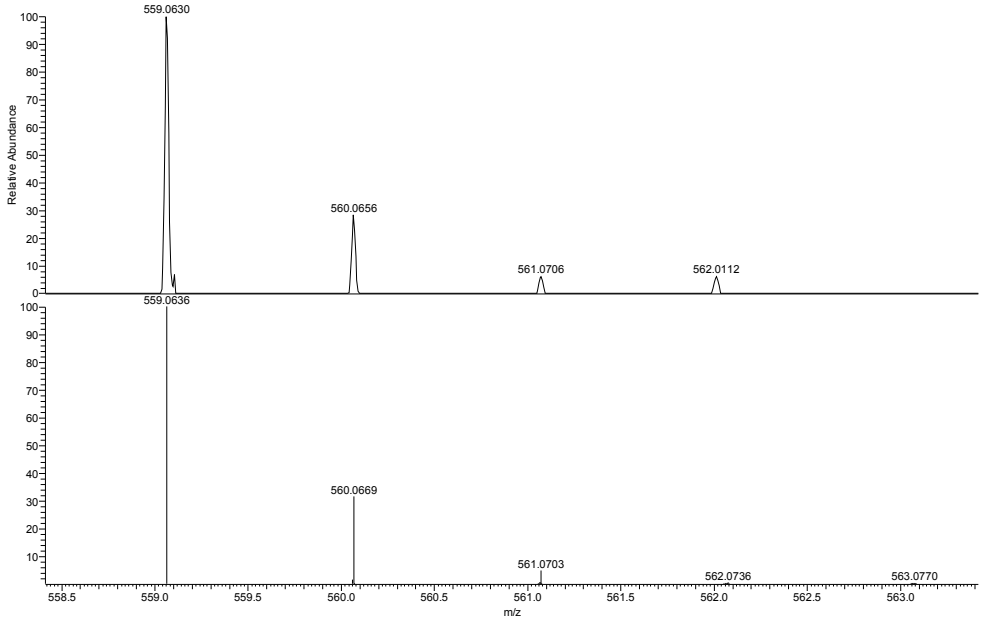

Fig. S16 High-resolution ESI mass spectrum of **1**: Experimental (top) and theoretical (bottom) isotope patterns of $[C_{29}H_{19}N_4O_2Rh+H]^+$.

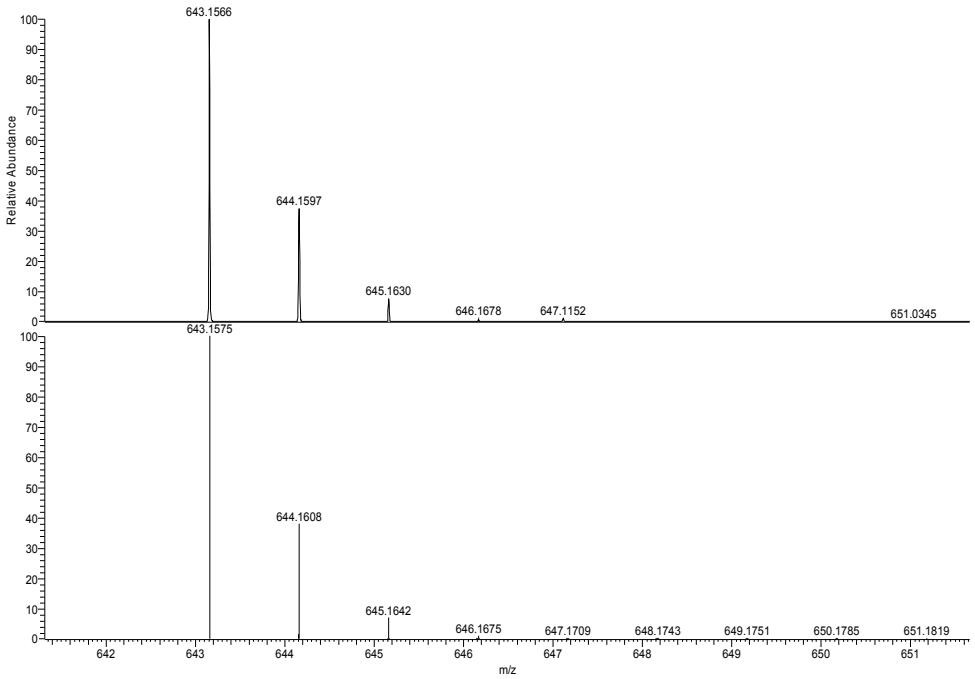

Fig. S17 High-resolution ESI mass spectrum of **2**: Experimental (top) and theoretical (bottom) isotope patterns of $[C_{35}H_{31}N_4O_2Rh+H]^+$.

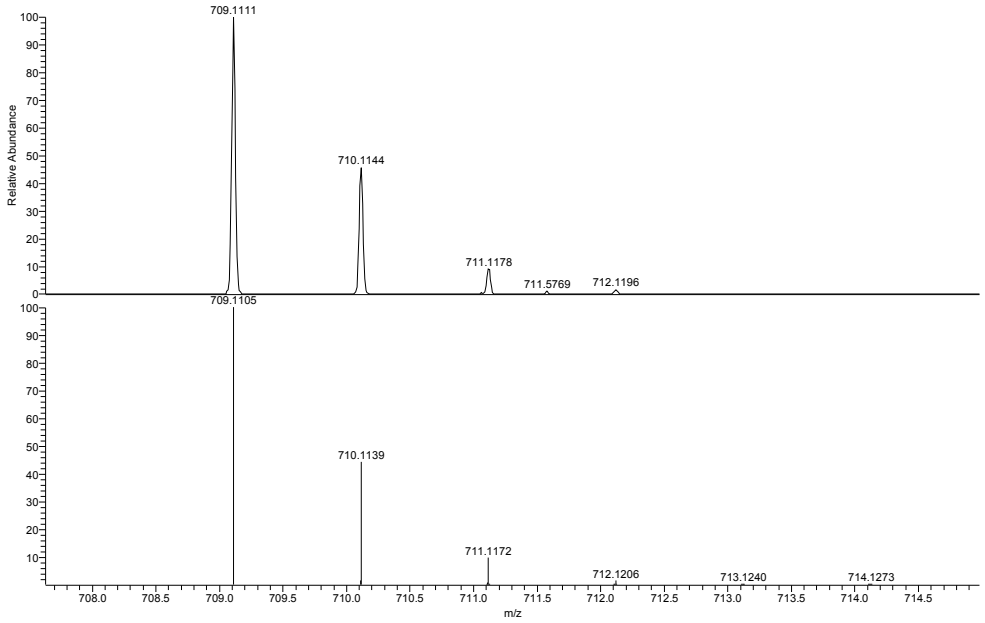

Fig. S18 High-resolution ESI mass spectrum of **3**: Experimental (top) and theoretical (bottom) isotope patterns of $[C_{41}H_{25}N_4O_2Rh+H]^+$.

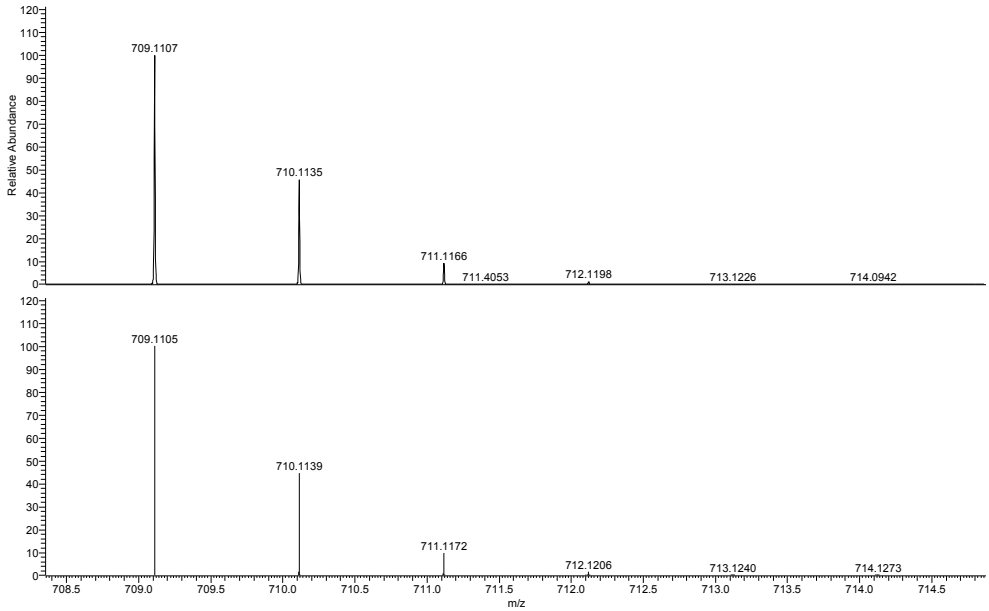

Fig. S19 High-resolution ESI mass spectrum of **4**: Experimental (top) and theoretical (bottom) isotope patterns of $[C_{41}H_{25}N_4O_2Rh+H]^+$.

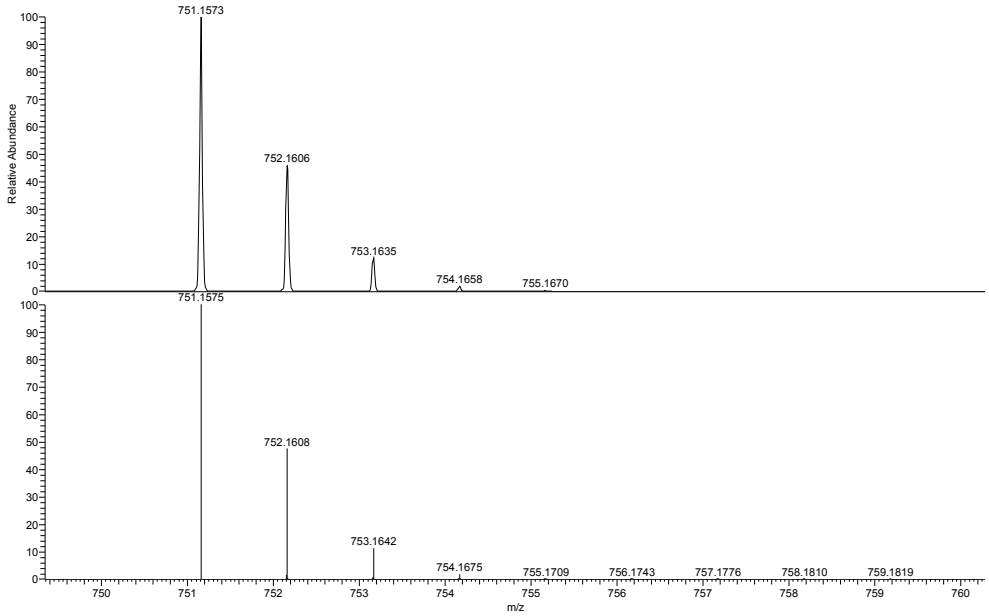

Fig. S20 High-resolution ESI mass spectrum of **5**: Experimental (top) and theoretical (bottom) isotope patterns of $[C_{44}H_{31}N_4O_2Rh+H]^+$.

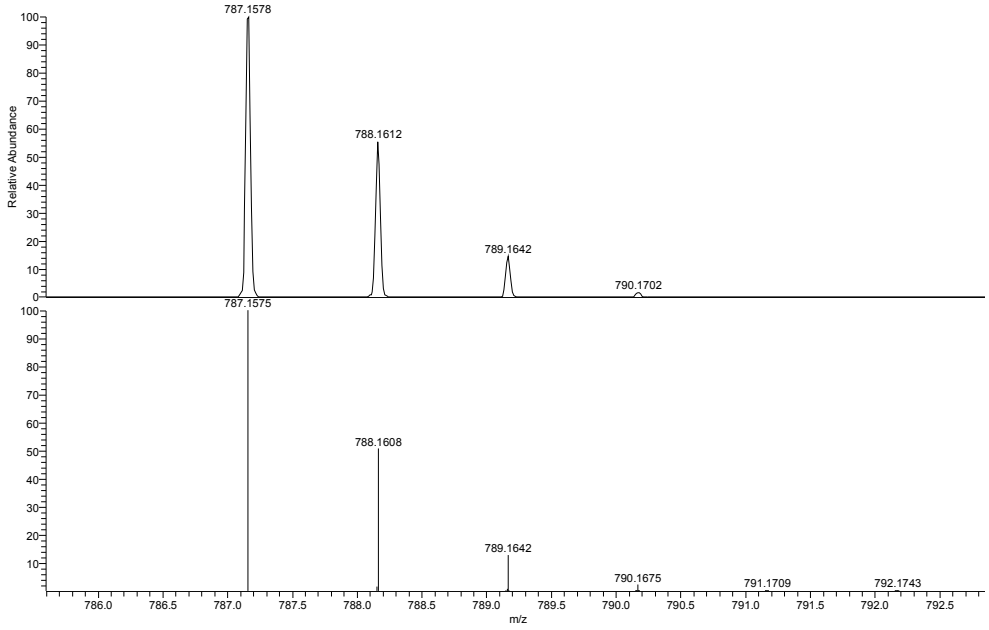

Fig. S21 High-resolution ESI mass spectrum of **6**: Experimental (top) and theoretical (bottom) isotope patterns of $[C_{47}H_{31}N_4O_2Rh+H]^+$.

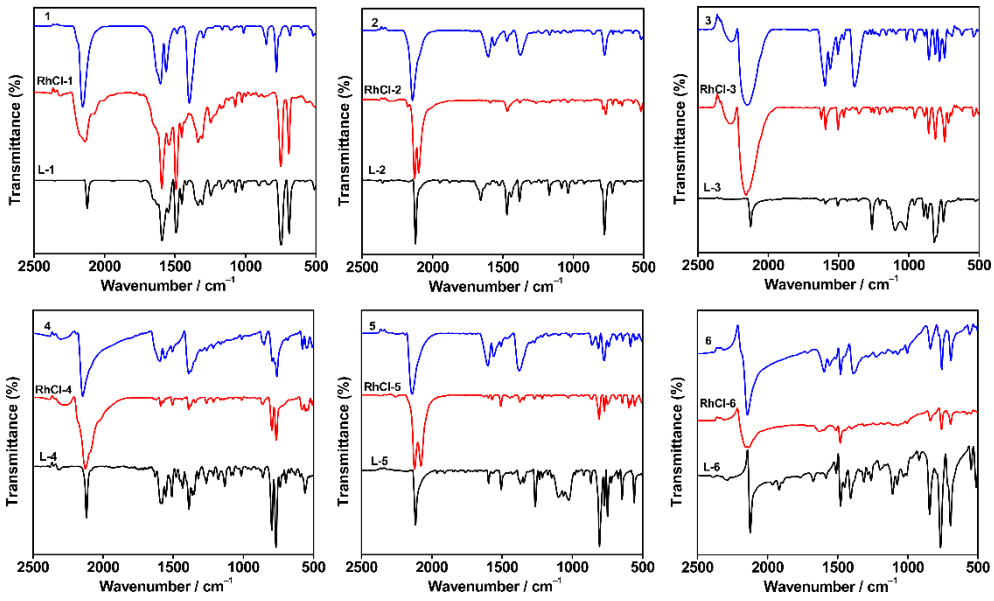

Fig. S22 FT-IR spectra of **L-1**−**L-6**, **RhCl-1**−**RhCl-6**, and **1**−**6**.

2.2 Aggregation Behavior in Neat Solvents

2.2.1 Photophysical Properties in dilute solution

The luminescence quantum yields of the monomeric emissions of zwitterions **1**−**6** were estimated to be 0.022−0.074% using $[Ru(bpy)_3]Cl_2$ (Φ = 0.042) as the reference. And the monomeric emission lifetimes of the dilute solutions were not detected in the microsecond regime.

Table S1. Photophysical data of **1**−**6** in methanol or DMSO solutions

Complex	Solvent	Absorption λ_{max}/nm (ε/L·mol^{-1}·cm^{-1})	Emission λ_{em}/nm	Φ/% [c]
1	MeOH	336 (33,800) [a], 415 (3,400) [a], 466 (725) [a] 544 [b]	531 [a]	0.022
	DMSO	343 (7,125) [a], 413 (7,125) [a], 472 (350) [a] 545 [b]	531 [a]	0.062
2	MeOH	338 (35,720) [a], 413 (4,320) [a], 463 (940) [a] 553 [b], 685 [b]	530 [a] 714 [b]	0.025
	DMSO	340 (35,412) [a], 413 (4,975) [a], 463 (788) [a] 558 [b]	529 [a] 720 [b]	0.058
3	MeOH	339 (27,400) [a], 413 (2,775) [a], 467 (650) [a] 569 [b], 685 [b]	532 [a]	0.013
	DMSO	343 (17,960) [a], 413 (2,440) [a], 471 (720) [a] 575 [b], 698 [b]	531 [a]	0.065
4	MeOH	341 (11,283) [a], 415 (2,566) [a], 466 (1350) [a] 575 [b], 724 [b]	532 [a] 734 [b]	0.04
	DMSO	350 (30,260) [a], 417 (4,000) [a], 471 (880) [a] 582 [b], 745 [b]	530 [a] 745 [b]	0.072
5	MeOH	353 (32,000) [a], 416 (4,620) [a], 467 (1,000) [a] 577 [b], 690 [b]	529 [a] 707 [b]	0.039
	DMSO	355 (25,420) [a], 412 (3,980) [a], 467 (1,120) [a] 574 [b], 728 [b]	531 [a] 1120 [b], 1215 [b]	0.064
6	MeOH	337 (30,512) [a], 411 (2,850) [a], 469 (712) [a] 568 [b]	532 [a]	0.015
	DMSO	340 (26,380) [a], 413 (3,040) [a], 471(513) [a] 570 [b], 690 [b]	530 [a]	0.074

[a] The UV−vis absorption and emission spectra of **1**−**6** with a monomer state in methanol or DMSO at a dilute concentration of 5.0×10^{-5} mol L^{-1}. [b] The low-energy absorption and emission bands of **1**−**6** with an aggregation state at a high concentration of 1.0×10^{-3} mol L^{-1}. [c] Luminescence quantum yields (Φ) of the monomer state were estimated by using $[Ru(bpy)_3]Cl_2$ (in water, Φ = 0.040) as the reference.[S6,S7]

2.2.2 Concentration-Dependent UV−vis Absorption and Emission Studies

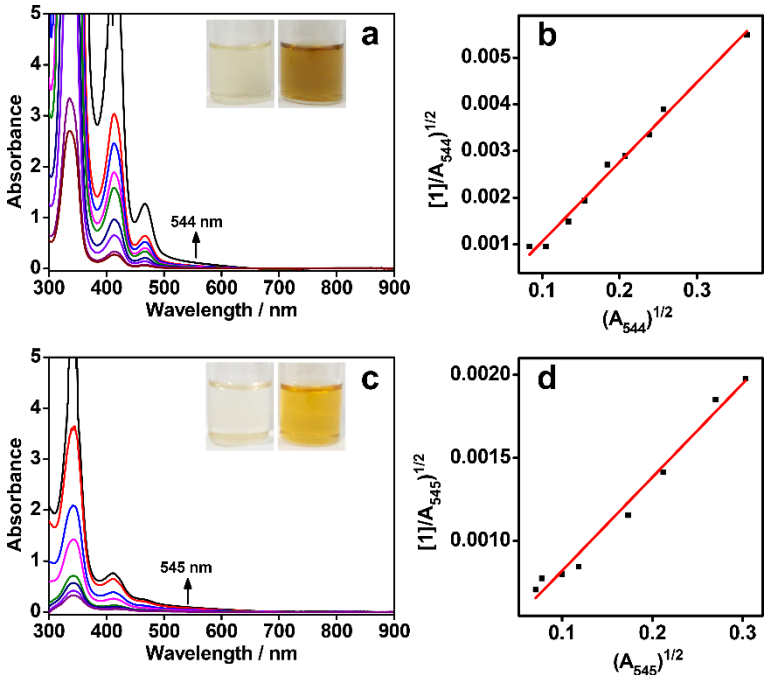

Fig. S23 Concentration-dependent UV−vis spectra of **1** in methanol (a and b) and DMSO (c and d) at room temperature. From bottom to top: (a) 5.0×10^{-5}, 1.0×10^{-4}, 2.0×10^{-4}, 3.0×10^{-4}, 4.0×10^{-4}, 6.0×10^{-4}, 8.0×10^{-4}, 1.0×10^{-3}, 2.0×10^{-3} mol L^{-1}; (c) 5.0×10^{-5}, 6.0×10^{-5}, 8.0×10^{-5}, 1.0×10^{-4}, 2.0×10^{-4}, 5.0×10^{-4}, 8.0×10^{-4}, 1.0×10^{-3} mol L^{-1}.The dimerization (b and d) plots were obtained with monomer−dimer equilibriums by monitoring the dimeric absorption bands. Insets: The dilute solutions of **1** in methanol (a) and DMSO (c, 5.0×10^{-5} mol L^{-1}) were light yellow, while at a high concentration of 1.0×10^{-3} mol L^{-1}, the solutions changed to brow yellow (a) and yellow (c).

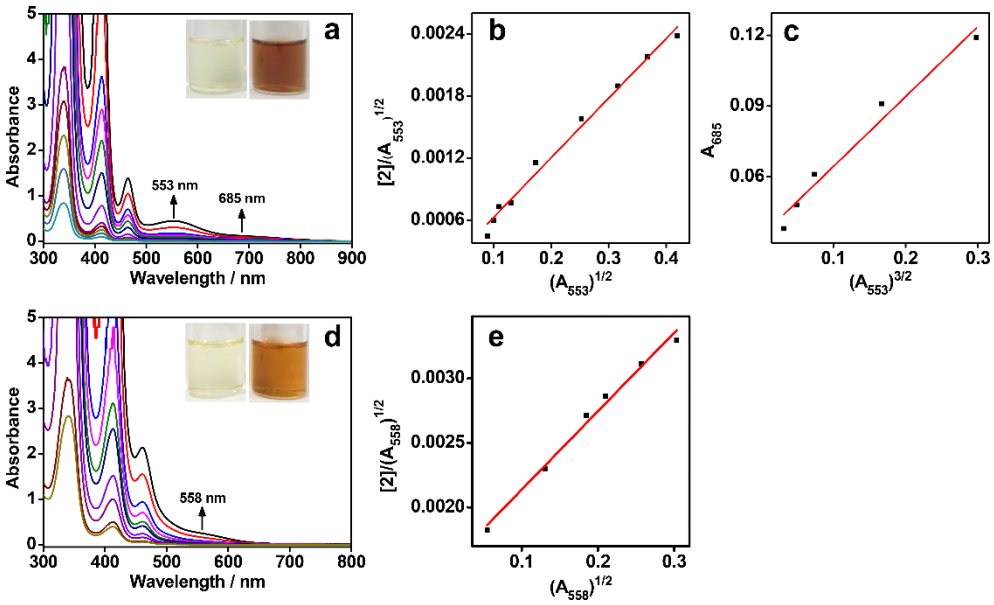

Fig. S24 Concentration-dependent UV−vis spectra of **2** in methanol (a, b, and c) and DMSO (d and e) at room temperature. From bottom to top: (a) 5.0×10^{-5}, 6.0×10^{-5}, 8.0×10^{-5}, 1.0×10^{-4}, 2.0×10^{-4}, 4.0×10^{-4}, 6.0×10^{-4}, 8.0×10^{-4}, 1.0×10^{-3}, 1.5×10^{-3}, 2.0×10^{-3} mol L^{-1}; (d) 5.0×10^{-5}, 1.0×10^{-4}, 2.0×10^{-4}, 3.0×10^{-4}, 4.0×10^{-4}, 6.0×10^{-4}, 8.0×10^{-4}, 1.0×10^{-3}, 1.5×10^{-3}, 2.0×10^{-3} mol L^{-1}. The dimerization (b and e) and trimerization (c) plots were obtained with monomer−dimer and (monomer + dimer)−trimer equilibriums by monitoring the dimeric and trimeric absorption bands, respectively. Insets: The dilute solutions of **2** in methanol (a) and DMSO (c, 5.0×10^{-5} mol L^{-1}) were light yellow, while at a high concentration of 1.0×10^{-3} mol L^{-1}, both the solutions changed to brow yellow (a and c).

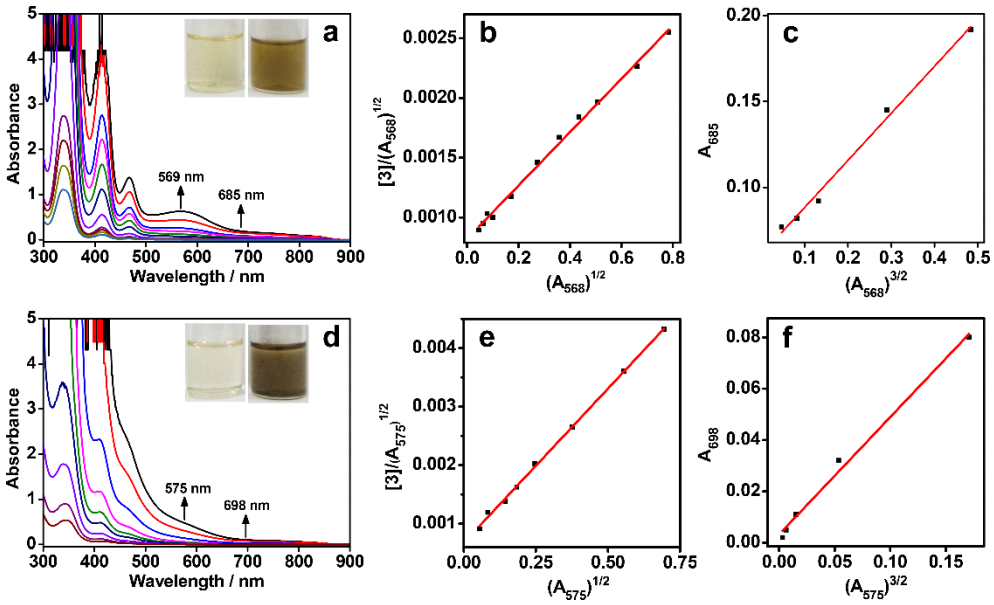

Fig. S25 Concentration-dependent UV−vis spectra of **3** in methanol (a, b, and c) and DMSO (d, e, and f) at room temperature. From bottom to top: (a) 5.0×10^{-5}, 6.0×10^{-5}, 8.0×10^{-5}, 1.0×10^{-4}, 2.0×10^{-4}, 4.0×10^{-4}, 6.0×10^{-4}, 8.0×10^{-4}, 1.0×10^{-3}, 1.5×10^{-3}, 2.0×10^{-3} mol L^{-1}; (d) 5.0×10^{-5}, 1.0×10^{-4}, 2.0×10^{-4}, 3.0×10^{-4}, 5.0×10^{-4}, 8.0×10^{-4}, 1.0×10^{-3}, 1.5×10^{-3}, 2.0×10^{-3} mol L^{-1}. The dimerization (b and e) and trimerization (c and f) plots were obtained with monomer−dimer and (monomer + dimer)−trimer equilibriums by monitoring the dimeric and trimeric absorption bands, respectively. Insets: The dilute solutions of **3** in methanol (a) and DMSO (d, 5.0×10^{-5} mol L^{-1}) were light yellow, while at a high concentration of 1.0×10^{-3} mol L^{-1}, both the solutions changed to brow (a and d).

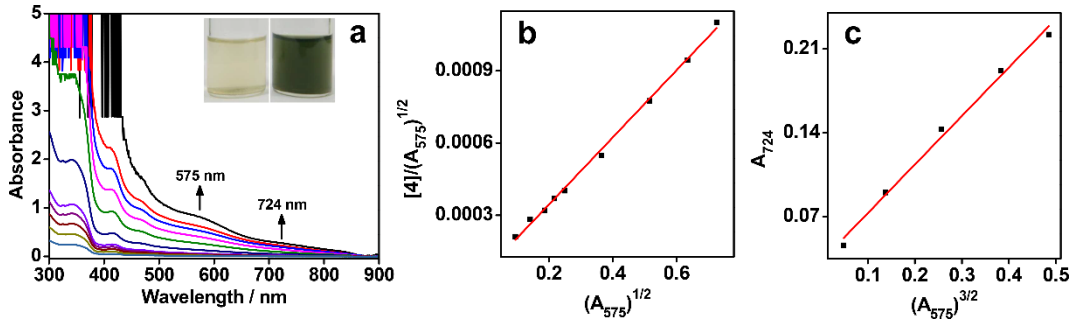

Fig. S26 Concentration-dependent UV−vis spectra of **4** in methanol (a, b, and c) at room temperature. From bottom to top: 3.0×10^{-5}, 5.0×10^{-5}, 6.0×10^{-5}, 8.0×10^{-5}, 1.0×10^{-4}, 2.0×10^{-4}, 4.0×10^{-4}, 6.0×10^{-4}, 8.0×10^{-4}, 1.0×10^{-3}, 2.0×10^{-3} mol L^{-1}. The dimerization (b) and trimerization (c) plots were obtained with monomer−dimer and (monomer + dimer)−trimer equilibriums by monitoring the dimeric and trimeric absorption bands, respectively. Insets: The dilute solutions of **4** in methanol (a, 5.0×10^{-5} mol L^{-1}) were light yellow, while at a high concentration of 1.0×10^{-3} mol L^{-1}, the solution changed to blackish green.

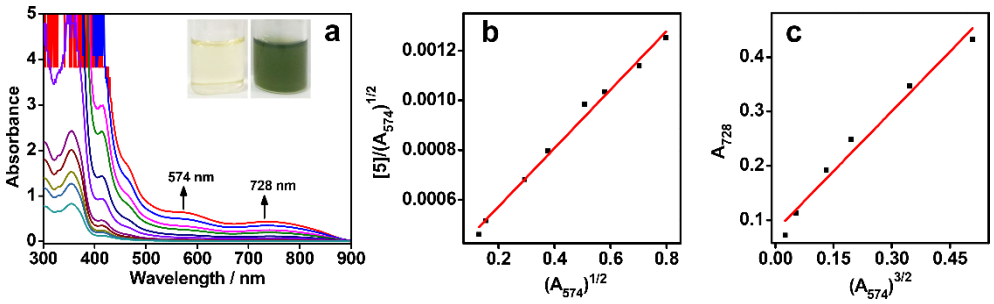

Fig. S27 Concentration-dependent UV−vis spectra of **5** in DMSO (a, b, and c) at room temperature. From bottom to top: 3.0×10^{-5}, 5.0×10^{-5}, 6.0×10^{-5}, 8.0×10^{-5}, 1.0×10^{-4}, 2.0×10^{-4}, 3.0×10^{-4}, 5.0×10^{-4}, 6.0×10^{-4}, 8.0×10^{-4}, 1.0×10^{-3} mol L^{-1}.The dimerization (b) and trimerization (c) plots were obtained with monomer−dimer and (monomer + dimer)−trimer equilibriums by monitoring the dimeric and trimeric absorption bands, respectively. Insets: The dilute solutions of **5** in methanol (a, 5.0×10^{-5} mol L^{-1}) were light yellow, while at a high concentration of 1.0×10^{-3} mol L^{-1}, the solution changed to green.

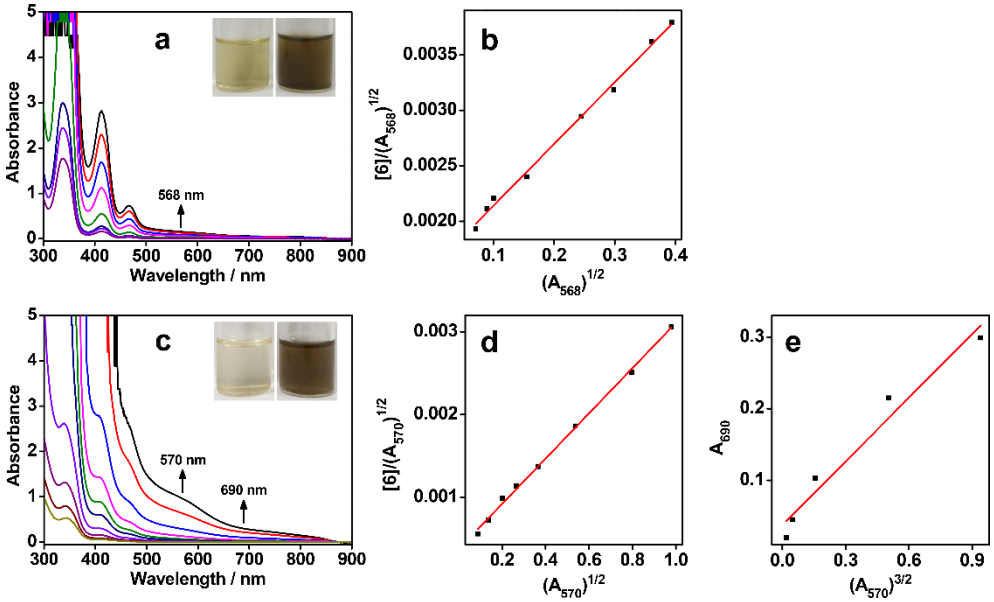

Fig. S28 Concentration-dependent UV−vis spectra of **6** in methanol (a and b) and DMSO (c, d, and e) at room temperature. From bottom to top: (a) 5.0×10^{-5}, 8.0×10^{-5}, 1.0×10^{-4}, 2.0×10^{-4}, 4.0×10^{-4}, 6.0×10^{-4}, 8.0×10^{-4}, 1.0×10^{-3} mol L^{-1}; (d) 5.0×10^{-5}, 1.0×10^{-4}, 2.0×10^{-4}, 3.0×10^{-4}, 4.0×10^{-4}, 6.0×10^{-4}, 8.0×10^{-4}, 1.0×10^{-3}, 1.5×10^{-3}, 2.0×10^{-3} mol L^{-1}. The dimerization (b and d) and trimerization (e) plots were obtained with monomer−dimer and (monomer + dimer)−trimer equilibriums by monitoring the dimeric and trimeric absorption bands, respectively. Insets: The dilute solutions of **6** in methanol (a) and DMSO (c, 5.0×10^{-5} mol L^{-1}) were light yellow, while at a high concentration of 1.0×10^{-3} mol L^{-1}, both the solutions changed to brow (a and c).

The rhodium(I) zwitterions of **1**−**6** existed as monomeric forms in the dilution solutions (5.0×10^{-5} mol L^{-1}), and exhibited monomeric emissions at ca. 530 nm (Fig. S29). Similar monomeric emissions were also captured in the dilute solutions of both bis(phenyisocyano)-rhodium(I)-diimine[8h] and tetrakis(phenylisocyano)-rhodium(I) complexes.[4b,8f] In the concentrated solutions (1.0×10^{-3} mol L^{-1}), Rh(I)···Rh(I) contacts formed between the zwitterions. Complexes **2**, **4**, and **5** with the different conjugated degree and steric hindrance of the ligands were found to display the dimeric emission bands at ca. 700−750 nm in methanol and/or DMSO (Fig. S30), which were assigned to dimeric 4dσ*(Rh_2) → 5pσ(Rh_2)/π*(isocyanide) excited states as a result of the Rh(I)···Rh(I) contacts.[4b,8f,9] Such dimeric emissions were also observed in the cases of tetrakis(phenylisocyano)-rhodium(I) complexes.[4b,8f,9] In the case of **2**, the six methyl groups probably led to a much stronger solvophobic, protective effect for favorable Rh(I)···Rh(I) interactions, while for **4**, the Rh(I)···Rh(I) interactions were assisted with strong π–π stacking interactions from the naphthalene ligands. Unexpectedly, two NIR-II emission bands appeared at 1120 and 1215 nm in the DMSO solution of **5** (Fig. S30), probably due to trimeric or oligomeric 4dσ*(Rh_n) → 5pσ(Rh_n)/π*(isocyanide) ($n \geq 3$) excited states. The NIR-II emissions arose from shorter Rh(I)···Rh(I) contacts, due to the methyl groups leading to a strong solvophobic, protective effect and the naphthalene ligands leading to strong π–π stacking interactions. No low-energy emissions for **1**, **3**, and **6** were observed, which were probably due to their ligand structures leading to the weakened π–π stacking interactions and solvophobic effect.

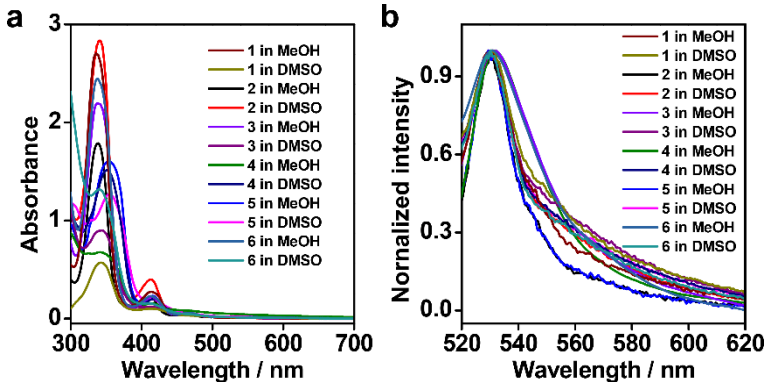

Fig. S29 The UV−vis absorption (a) and emission (b) spectra of **1**−**6** in methanol or DMSO at a concentration of 5.0×10^{-5} mol L^{-1}, wherein the zwitterions were in the monomeric state.

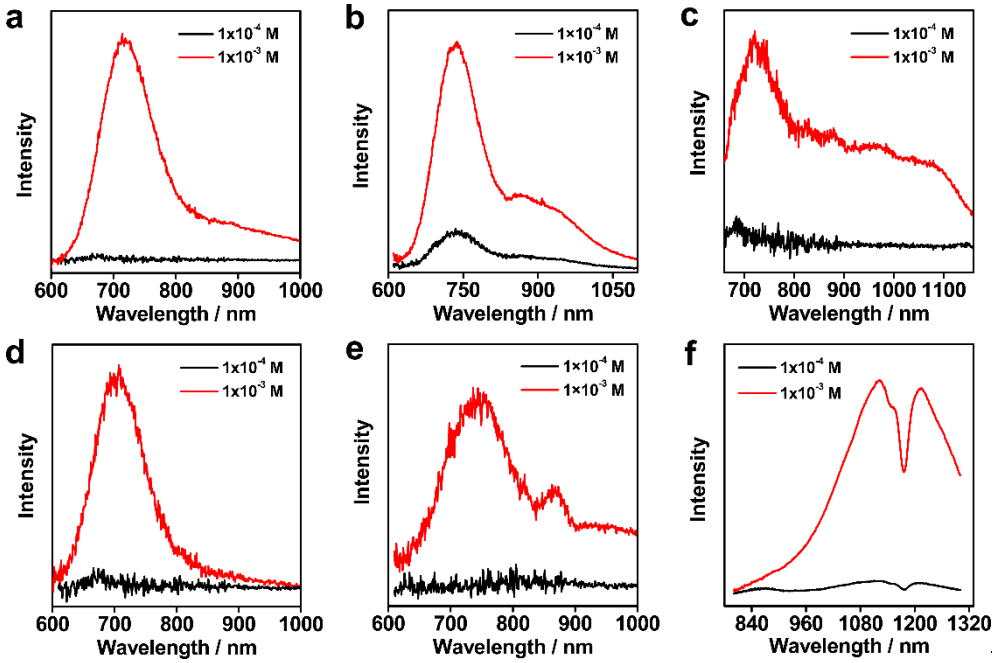

Fig. S30 Emission spectra of **2** (a and d), **4** (b and e), and **5** (c and f) in methanol (a−c) and DMSO (d−f) at concentrations of 1.0×10^{-4} (black line) and 1.0×10^{-3} mol L^{-1} (red line).

Table S2. Association constants (log *K*) of zwitterionic isocyanorhodium(I) complexes for concentration-dependent studies [a]

Zwitterion	Solvent	log K_d[b]	log K_t[c]	ΔG_d[d] (kJ mol^{-1})	ΔG_t[e] (kJ mol^{-1})
1	methanol	4.32	–[f]	−24.62	–
	DMSO	4.63	–[f]	−26.39	–
2	methanol	6.09	2.67	−34.71	−15.26
	DMSO	3.11	–[f]	−17.76	–
3	methanol	3.09	2.35	−17.65	−13.39
	DMSO	3.76	2.66	−21.48	−15.15
4	methanol	5.21	3.61	−29.71	−20.62
	DMSO	3.61	2.42	−20.57	−13.81
5	methanol	3.20	2.72	−18.25	−15.54
	DMSO	3.72	3.16	−21.20	−18.03
6	methanol	3.05	–[f]	−17.38	–
	DMSO	3.99	2.72	−22.77	−15.53

[a] Association constants are determined in the concentration range of 5×10^{-5} to 2×10^{-3} M in methanol or DMSO solution from UV−vis absorption studies. [b] Dimerization constant determined from dimerization plot of the monomer−dimer equilibrium. [c] Trimerization constant determined from trimerization plot of the dimer−trimer equilibrium. [d] $\Delta G_d = -RT \ln K_d$. [e] $\Delta G_t = -RT \ln K_t$. [f] Trimeric absorption band cannot be observed.

2.2.3 Temperature-Dependent UV−vis Absorption Studies

To obtain additional mechanistic insights into the aggregation processes of Zwitterions **1**−**6**, all of the methanol solutions were further subjected to temperature-dependent UV−vis absorption spectral studies. Upon increasing the temperature from 278 to 332 K, both the dimeric and trimeric absorption bands exhibited a gradual decrease in intensity, indicative of the deaggregation of the zwitterions (Fig. S31−S36). The plots of the normalized degree of aggregation at the dimeric absorptions relative to the temperature was shown to generate a set of clear sigmoidal curves, characteristic of an isodesmic self-assembly mechanism involving a non-nucleated aggregation pathway.[S10−S14] The isodesmic fitting gave a melting temperature (T_m) and an enthalpy change (ΔH), as summarized in Table S3. The ΔH values were rather negative, which was again due to the zwitterionic aggregation arising from Rh(I)···Rh(I) and π−π stacking interactions. The larger enthalpy releases of 4 and 2 were consistent with the aforementioned stronger π–π stacking interaction and solvophobic effect, respectively, whereas the least negative ΔH value of 6 were due to the most steric hindrance of 1,1′-biphenyl groups leading to weakened π−π stacking interactions therein.

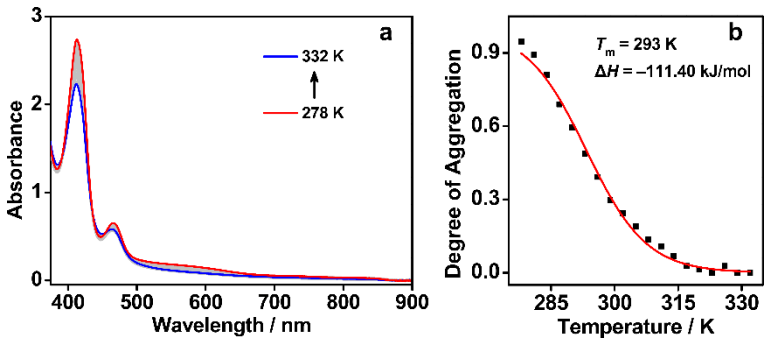

Fig. S31 (a) Temperature-dependent UV−vis absorption spectral changes of **1** (methanol, 5×10^{-4} mol L^{-1}, 278−332 K). (b) Plot of the degree of aggregation (black dot) at 545 nm as a function of temperature and its fitting curve (red line) of **1**.

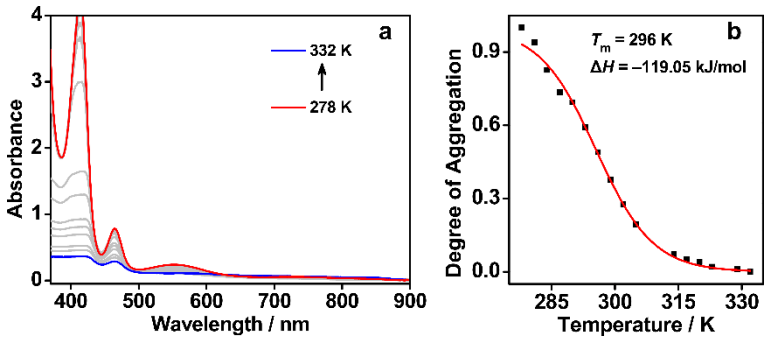

Fig. S32 (a) Temperature-dependent UV−vis absorption spectral changes of **2** (methanol, 5×10^{-4} mol L^{-1}, 278−332 K). (b) Plot of the degree of aggregation (black dot) at 551 nm as a function of temperature and its fitting curve (red line) of **2**.

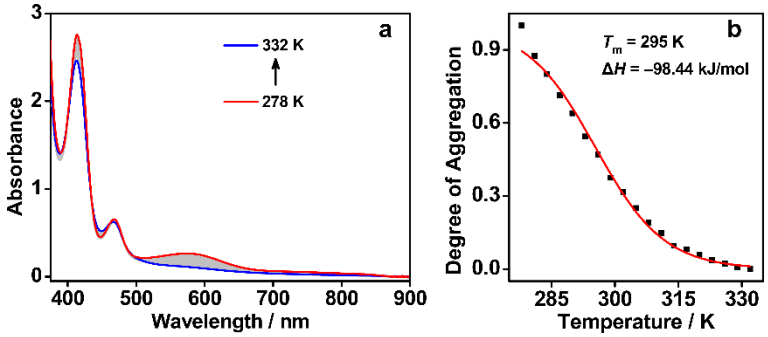

Fig. S33 (a) Temperature-dependent UV−vis absorption spectral changes of **3** (methanol, 5×10^{-4} mol L^{-1}, 278−332 K). (b) Plot of the degree of aggregation (black dot) at 570 nm as a function of temperature and its fitting curve (red line) of **3**.

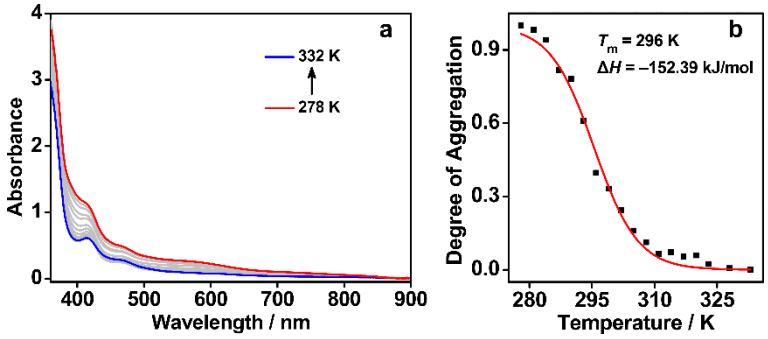

Fig. S34 (a) Temperature-dependent UV−vis absorption spectral changes of **4** (methanol, 5×10^{-4} mol L^{-1}, 278−332 K). (b) Plot of the degree of aggregation (black dot) at 575 nm as a function of temperature and its fitting curve (red line) of **4**.

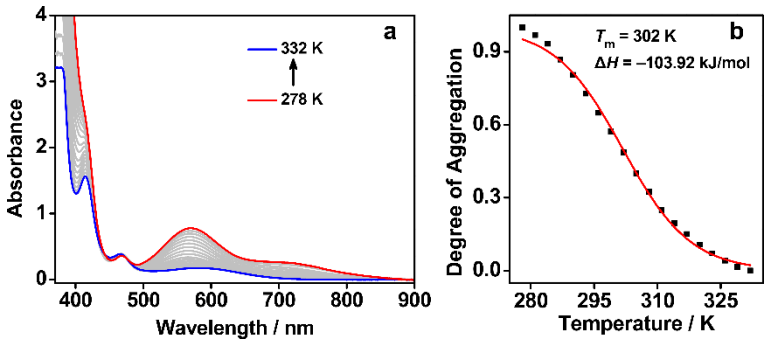

Fig. S35 (a) Temperature-dependent UV−vis absorption spectral changes of **5** (methanol, 5×10^{-4} mol L^{-1}, 278−332 K). (b) Plot of the degree of aggregation (black dot) at 572 nm as a function of temperature and its fitting curve (red line) of **5**.

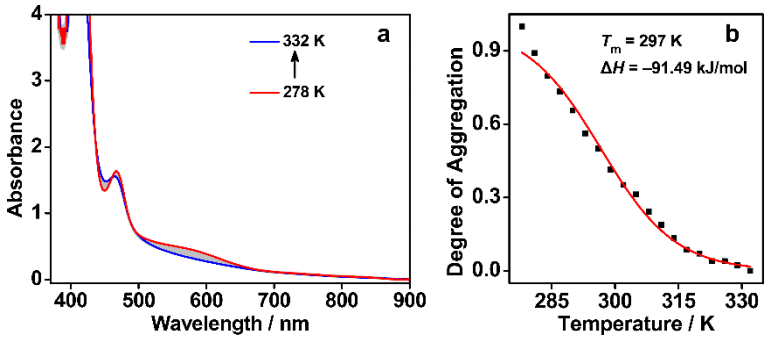

Fig. S36 (a) Temperature-dependent UV−vis absorption spectral changes of **6** (methanol, 5×10^{-4} mol L^{-1}, 278−332 K). (b) Plot of the degree of aggregation (black dot) at 570 nm as a function of temperature and its fitting curve (red line) of **6**.

Table S3. Temperature-dependent UV−vis absorption atudies of isocyanorhodium(I) zwitterions

Zwitterion	Solvent	T_m [a] (K)	ΔH [a] (kJ mol^{-1})
1	methanol	293	−111.40
2	methanol	296	−119.05
3	methanol	295	−98.44
4	methanol	296	−152.39
5	methanol	302	−103.92
6	methanol	297	−91.49

[a] The melting temperature T_m and enthalpy release ΔH were determined by fitting the absorption spectral changes with the temperature-dependent isodesmic model.

2.2.4 Concentration-Dependent ^{1}H NMR Studies

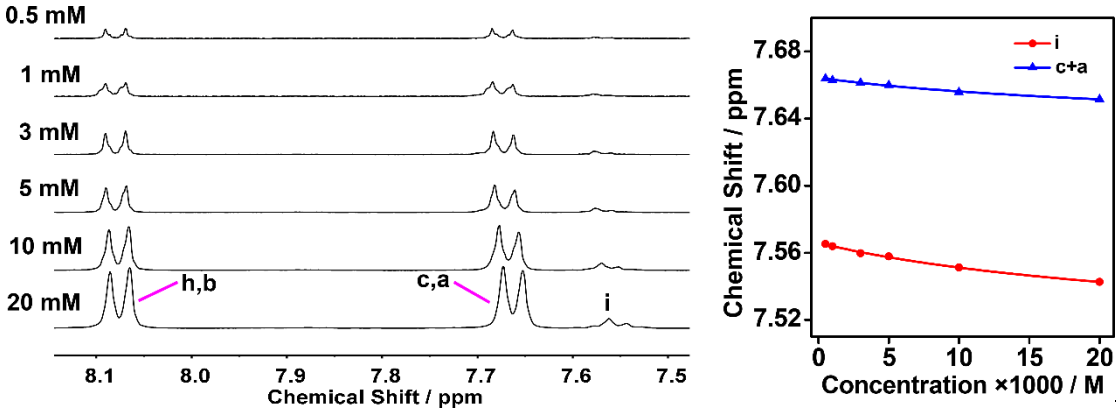

Fig. S37 ^{1}H NMR spectra of **1** with increasing the concentration in CD_3OD at room temperature (left). The corresponding plot of chemical shift against the concentration fitted with the self-association model of monomer−dimer equilibrium (right). The proton assignments were shown in Fig. S4.

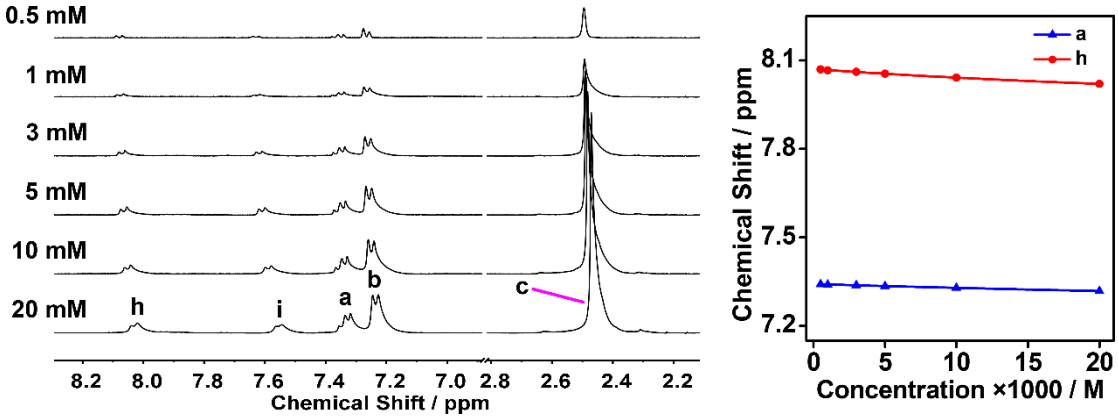

Fig. S38 ^{1}H NMR spectra of **2** with increasing the concentration in CD_3OD at room temperature (left). The corresponding plot of chemical shift against the concentration fitted with the self-association model of monomer−dimer equilibrium (right). The proton assignments were shown in Fig. S5.

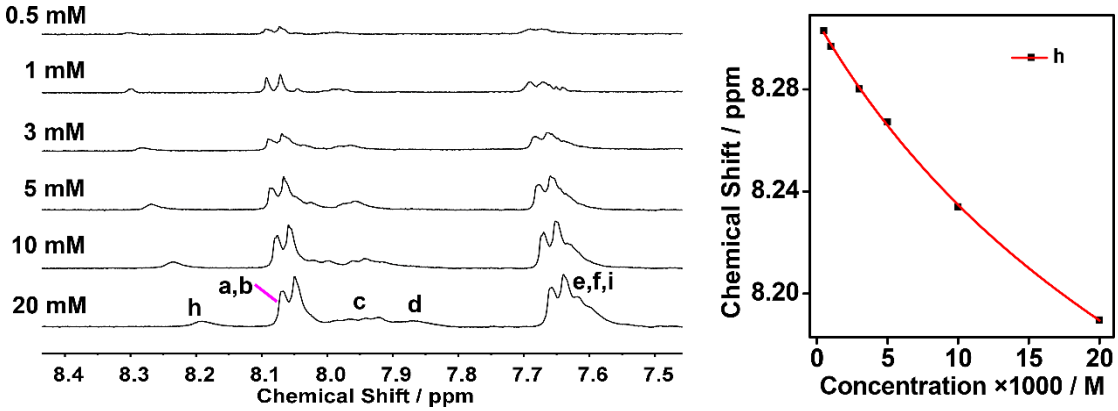

Fig. S39 ^{1}H NMR spectra of **3** with increasing the concentration in CD_3OD at room temperature (left). The corresponding plot of chemical shift against the concentration fitted with the self-association model of monomer−dimer equilibrium (right). The proton assignments were shown in Fig. S6.

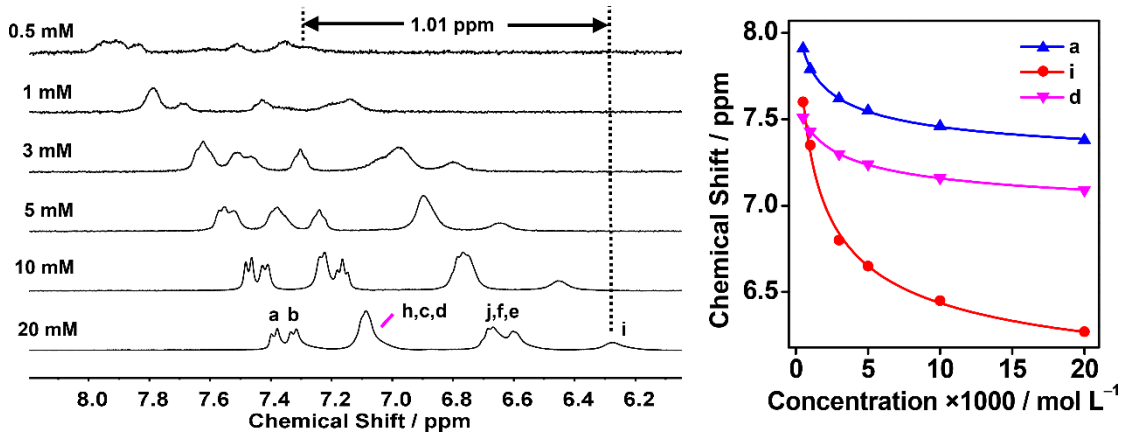

Fig. S40 ^{1}H NMR spectra of **4** with increasing the concentration in CD_3OD at room temperature (left). The corresponding plot of chemical shift against the concentration fitted with the self-association model of monomer−dimer equilibrium (right). The proton assignments were shown in Fig. S7.

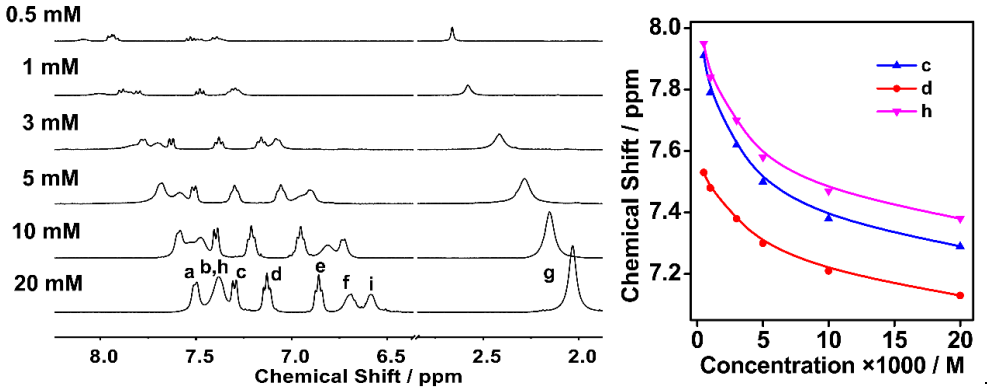

Fig. S41 ^{1}H NMR spectra of **5** with increasing the concentration in CD_3OD at room temperature (left). The corresponding plot of chemical shift against the concentration fitted with the self-association model of monomer−dimer equilibrium (right). The proton assignments were shown in Fig. S8

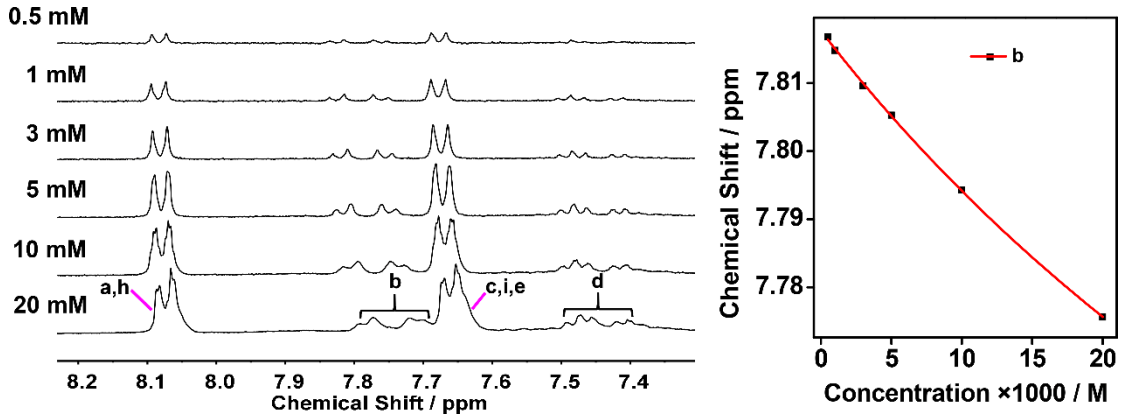

Fig. S42 ^{1}H NMR spectra of **6** with increasing the concentration in CD_3OD at room temperature (left). The corresponding plot of chemical shift against the concentration fitted with the self-association model of monomer−dimer equilibrium (right). The proton assignments were shown in Fig. S9.

Table S4. Concentration-dependent chemical shifts and association constants (log *K*) of zwitterionic isocyanorhodium(I) complexes [a]

Zwitterion	Proton	δ_d [b] (ppm)	δ_m [b] (ppm)	$\delta_d-\delta_m$ (ppm)	log K_a [b]
1	i	7.48	7.57	−0.09	1.07
2	h	7.74	8.07	−0.33	0.72
3	h	7.77	8.31	−0.54	0.96
4	a	7.22	8.37	−1.15	2.98
5	c	6.97	8.08	−1.11	2.34
6	i	7.46	7.67	−0.23	0.73

[a] Association constant determined from concentration-dependent ^{1}H NMR studies in the concentration range of 5×10^{-4} to 2×10^{-2} mol L^{-1} in CD_3OD solution. [b] The intrinsic chemical shifts of monomer (δ_m) and dimer (δ_d), and dimerization constant (log K_a) were determined by using NMR dimerization model. The molecular structure of **1**−**6** was shown in Fig. S5−S10, respectively.

2.2.5 Temperature-Dependent ^{1}H NMR Studies

Having analyzed the aggregation property of **1**−**6** at room temperature, we turned our attention to study their deaggregation behaviors by variable temperature ^{1}H NMR spectra. With increasing the temperature from 25 to 60 °C, the proton signals of **4** and **5** in CD_3OD at 1.0×10^{-2} mol L^{-1} showed clear downfield shifts ranging from $\Delta\delta = -0.19$ to −0.55 ppm (Fig. S46 and S47). These downfield shifts demonstrated that their π-stacking assemblies formed in the concentrated solutions at room temperature, and deaggregated gradually with increasing the temperature, which tallied with those of diluting the solutions, as mentioned above. Similar deaggregation processes were also captured in d^8 platinum(II)[S22−S24] and gold(III)[S13] complexes, wherein the well-resolved proton signals were observed at high temperature. However, in the present study, the proton signals became poorly resolved as broad peaks at 50 and 60 °C. This suggested that under these high temperature conditions, there still existed significant π–π stacking interactions between the rhodium(I) zwitterions, well explaining the much more negative Δ*H* values found in the above temperature-dependent UV−vis absorption spectroscopic studies (Fig. S34, S35, and Table S3). Such thermal induced aggregation behavior was similar to those lower critical solution temperature (LCST) phase transitions reported for both zwitterions[S25,S26] and polymeric zwitterions.[S27] Slight upfield shifts ($\Delta\delta = -0.04 \pm 0.01$) and broadening features in the cases of **1**−**3** and **6** were indicative of a recognizable increase in π−π stacking interactions at high temperature, again agreeing well with their much more negative Δ*H* values (Fig. S43−S45 and S48).

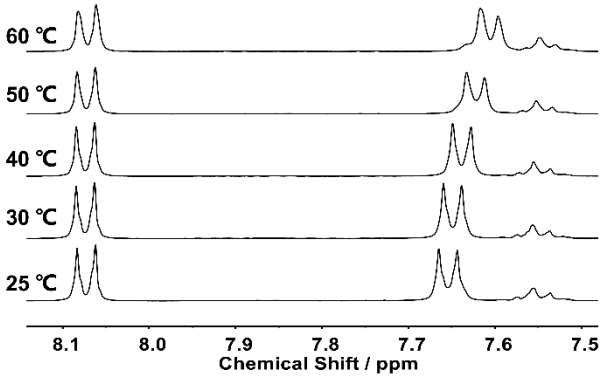

Fig. S43 Temperature-dependent ^{1}H NMR of **1** at 2.0×10^{-2} mol L^{-1} in CD_3OD. The proton assignments were shown in Fig. S4.

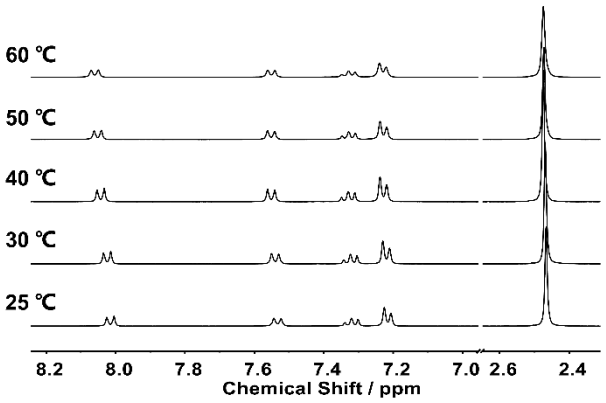

Fig. S44 Temperature-dependent ^{1}H NMR of **2** at 2.0×10^{-2} mol L^{-1} in CD_3OD. The proton assignments were shown in Fig. S5.

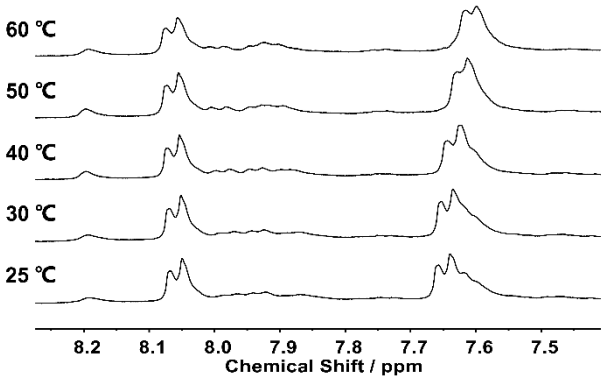

Fig. S45 Temperature-dependent ^{1}H NMR of **3** at 2.0×10^{-2} mol L^{-1} in CD_3OD. The proton assignments were shown in Fig. S6.

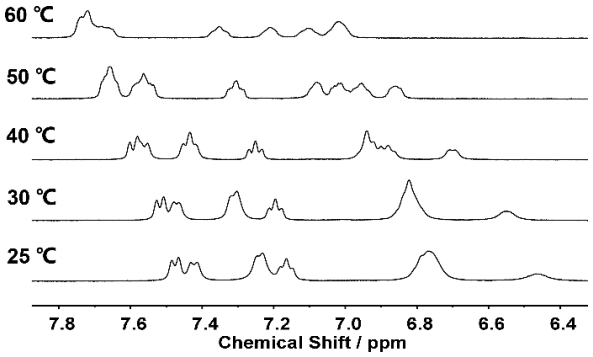

Fig. S46 Temperature-dependent ^{1}H NMR of **4** at 1.0×10^{-2} mol L^{-1} in CD_3OD. The proton assignments were shown in Fig. S7.

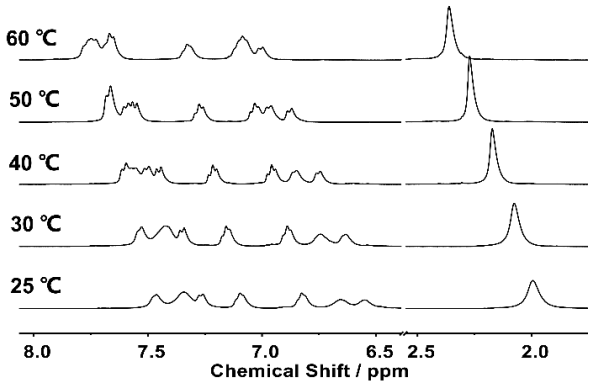

Fig. S47 Temperature-dependent ^{1}H NMR of **5** at 2.0×10^{-2} mol L^{-1} in CD_3OD. The proton assignments were shown in Fig. S8.

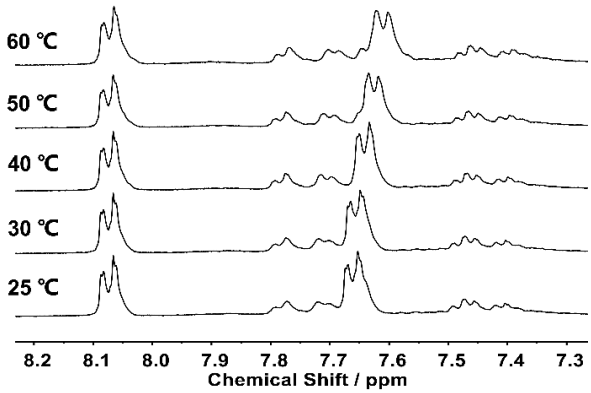

Fig. S48 Temperature-dependent ^{1}H NMR of **6** at 2.0×10^{-2} mol L^{-1} in CD_3OD. The proton assignments were shown in Fig. S9.

2.3 Solvent-Induced Supramolecular Aggregation and NIR-II Phosphorescence

Varying solvent compositions was found to be an effective strategy to induce the aggregation of d^8 rhodium(I),[S10,S12] gold(III)[S13] and platinum(II)[S14,S24] metal complexes. In this work, the strong aggregation propensity of the rhodium(I) zwitterions, together with their NIR-I/II emissions in methanol or DMSO at high concentrations, urged us to further screen the availability of the NIR-II phosphorescence behaviors in mixture solvents under dilute conditions.The addition of nonsolvents, such as water, acetonitrile, THF, and diethyl ether to the methanol or DMSO solutions of **1**−**6**, was used to evaluate their aggregation behaviors at room temperature.

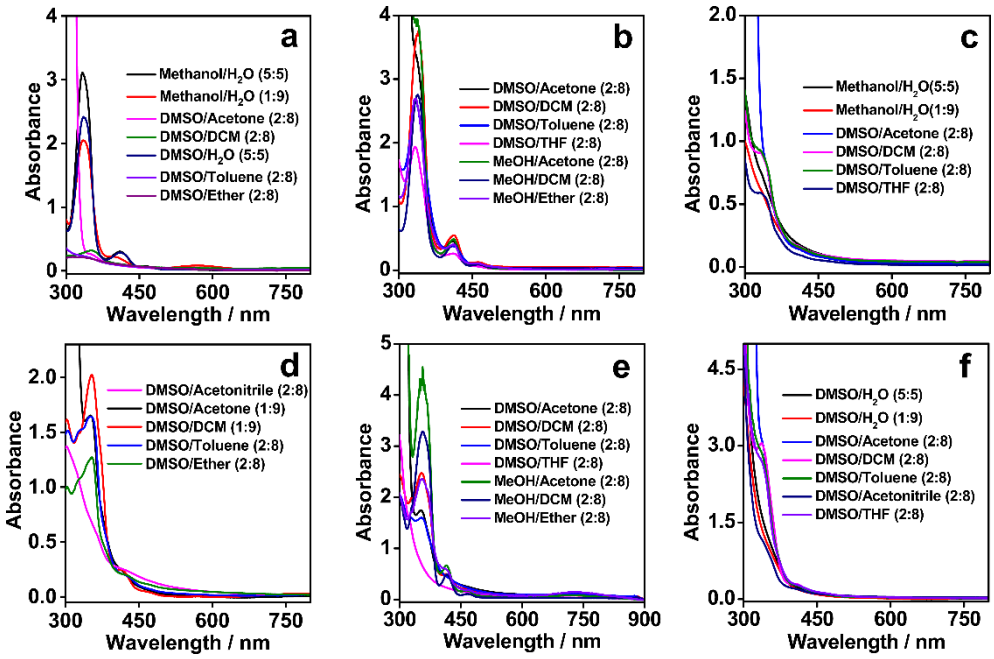

Fig. S49 The UV−vis absorption spectra of **1** (a), **2** (b), **3** (c), **4** (d), **5** (e), and **6** (f) under the different mixed solvent conditions at room temperature, wherein the concentration was controlled at 1.0×10^{-4} mol L^{-1}.

Table S5. Thermodynamic parameters for solvent induced supramolecular aggregation of **2** and **5**

Zwitterion	$\Delta G°$ (kJ mol^{-1})[a]	m (kJ mol^{-1})[a]	σ[a]
2	–37.07	26.90	1.00
5	–35.01	17.07	1.00

[a] Determined from curve fitting according to the nucleation elongation aggregation model from UV−vis absorption studies in methanol−water mixed solvents. $c_{tot} = 1 \times 10^{-4}$ mol L^{-1}, $n = 3$, $T = 298$ K.

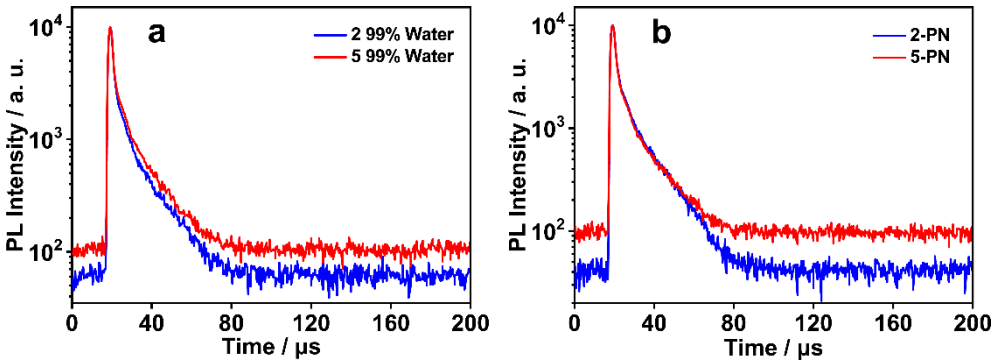

Fig. S50 Luminescence lifetime curves of **2** (99% water, a), **5** (99% water, a), **2-PN** (pure water, b), and **5-PN** (pure water, b).

The NIR-II emissions of **2**-99%, **5**-99%, **2-PN** and **5-PN** were assigned to ^{3}[4dσ*(Rh$_n$) → 5pσ(Rh$_n$)/π*(isocyanide), $n \geq 3$] excited states stemming from extended Rh(I)···Rh(I) contacts in aggregates. In fact, in the trimeric and oligomeric aggregates, the Rh(I)···Rh(I) distances is dynamic and unequal in solution. Such uneven Rh(I)···Rh(I) distances have been demonstrated by previously reported crystal structures, which have been well accepted in the community.[8d,8f,8i] In this context, one origin but two photoluminescence lifetimes appeared reasonably (τ_1 and τ_2), and thus probably originated from relatively long and short Rh(I)···Rh(I) distances in the aggregates, respectively.

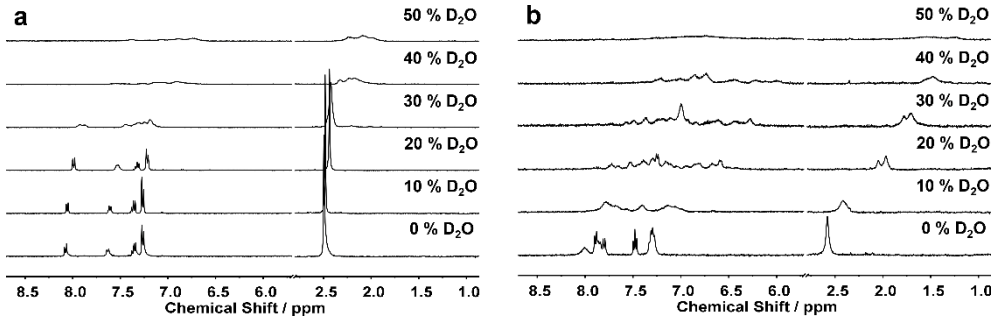

Fig. 51 ^{1}H NMR spectral curves of **2** (a) and **5** (b) at different volume content of D_2O in CD_3OD (1.0×10^{-3} mol L^{-1}, 400 MHz, 298 K).

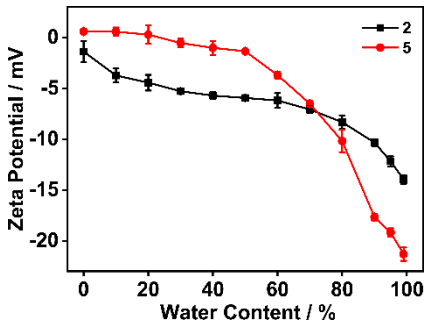

Fig. S52 Zeta potential evolution of **2** and **5** upon increasing water volume fraction in methanol (0, 10, 20, 30, 40, 50, 60, 70, 80, 90, 95, 99%, 1.0×10^{-4} mol L^{-1}).

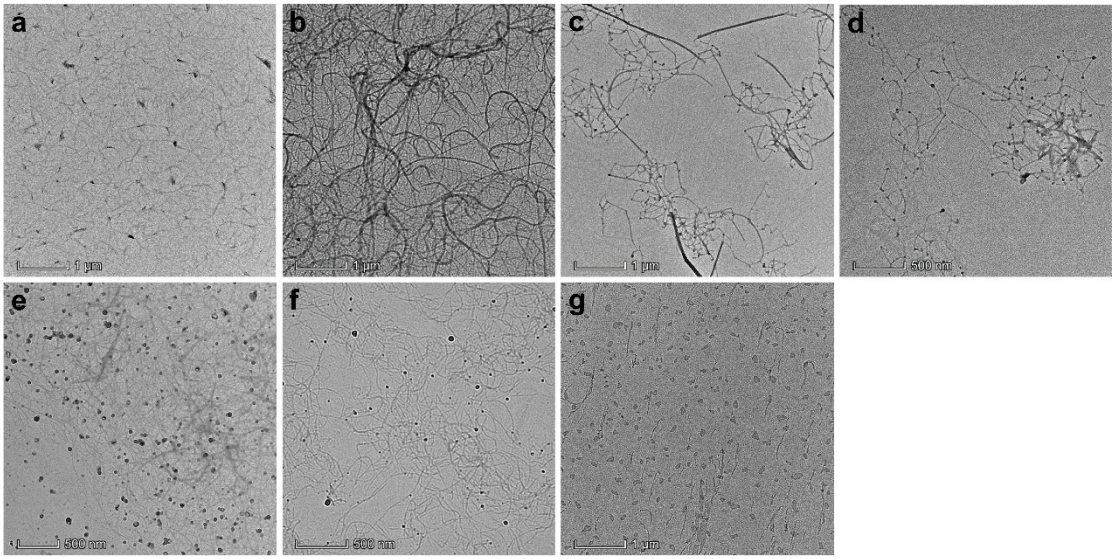

Fig. S53 Representative TEM images of **5** obtained in the methanol−water mixed solvents with 20% water (a), 30% water (b), 50% water (c), 60% water (d), 70% water (e), 80% water (f),and 95% water (g, 1.0×10^{-4} mol L^{-1}).

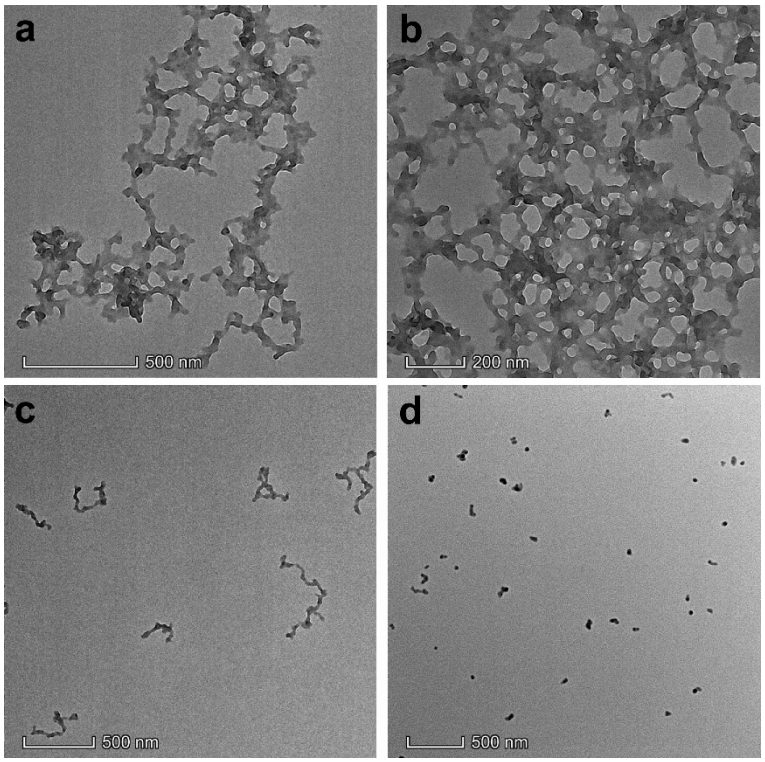

Fig. S54 Representative TEM images of **2** obtained in the methanol−water mixed solvents with 60% water (a), 70% water (b), 80% water (c), and 90% water (d, 1.0×10^{-4} mol L^{-1}).

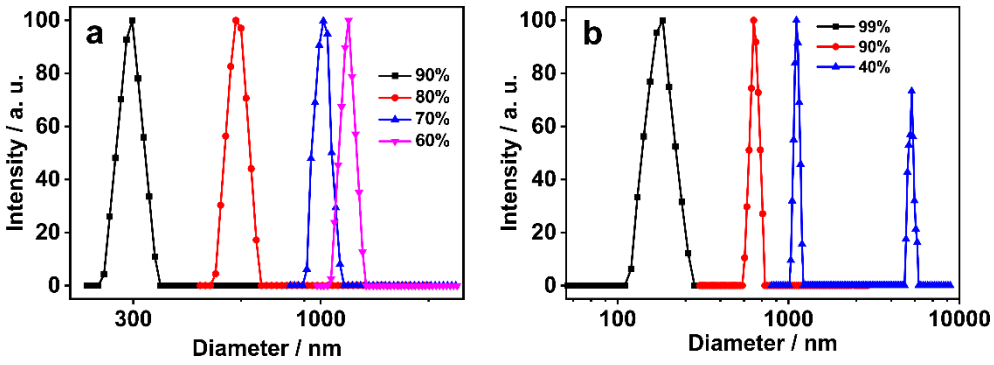

Fig. S55 Representative DLS traces of (a) **2** and (b) **5** in methanol−water mixed solvents with increasing the water content (1.0×10^{-4} mol L^{-1}).

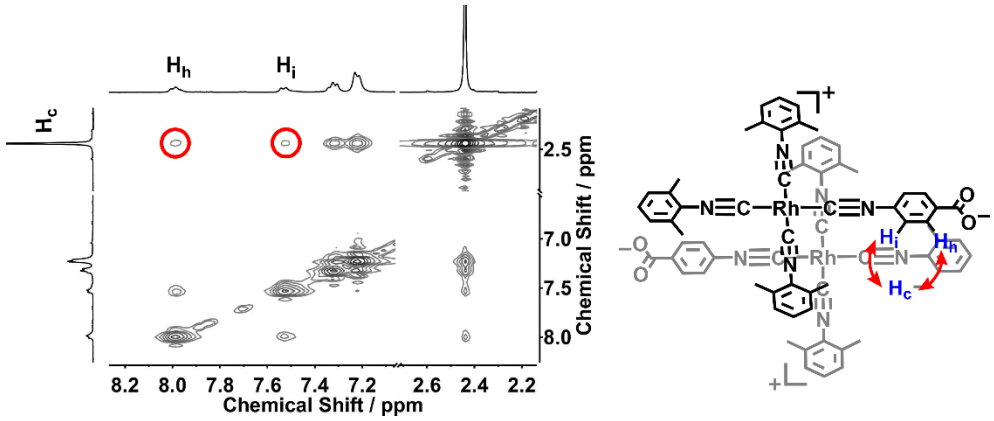

Fig. S56 $^{1}H-^{1}H$ NOESY spectrum of **2** in the CD_3OD-D_2O solvent mixture (v/v = 9/1, 2.0×10^{-3} mol L^{-1}, 400 MHz, 298 K)

2.4 WAXS patterns of 2-PN and 5-PN

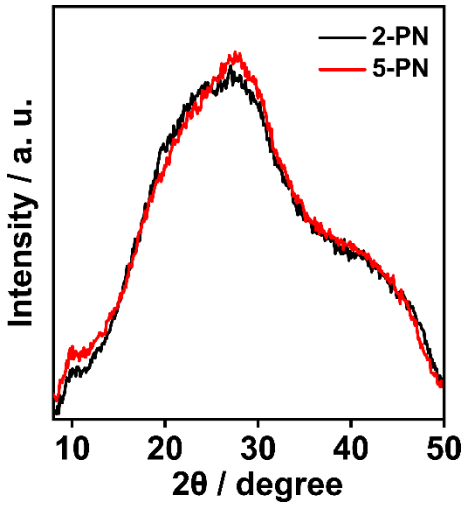

Fig. S57 WAXS patterns of **2-PN** and **5-PN** in water at 1.0×10^{-4} mol L^{-1}.

2.5 Biosafety assessment

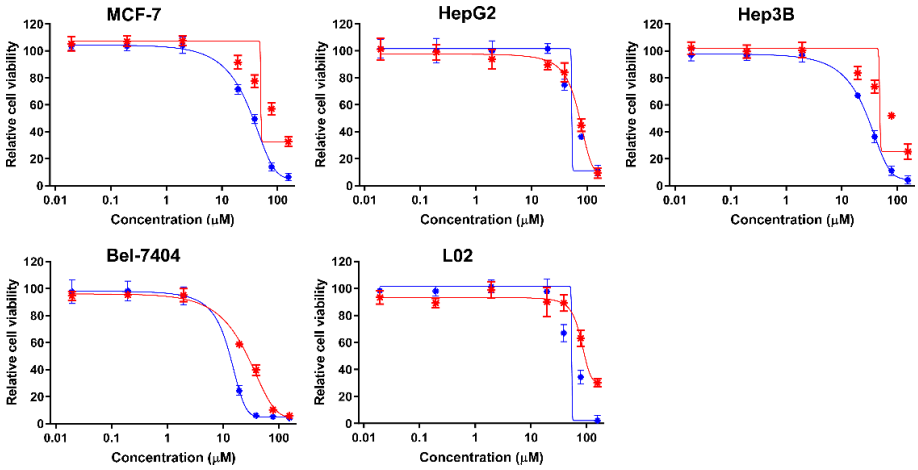

Fig. S58 Cell viability of various cells treated with **2-PN**.

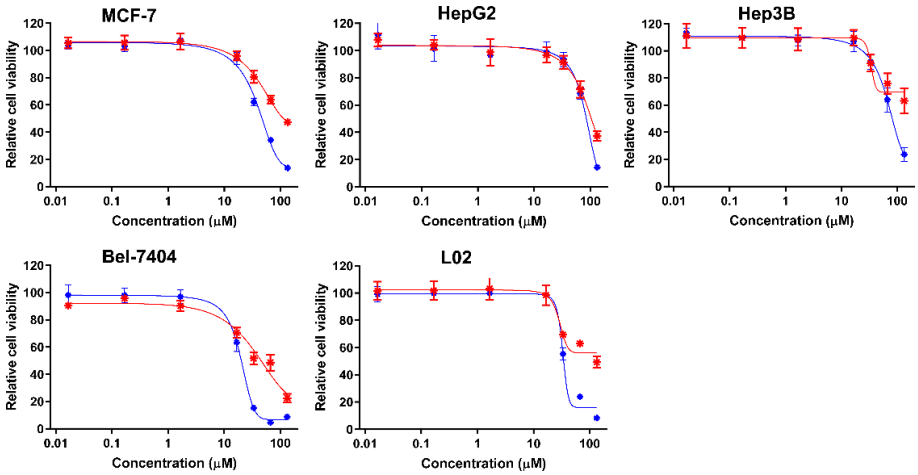

Fig. S59 Cell viability of various cells treated with **5-PN**.

Table S6 IC_{50} values of the polymer nanoparticles **2-PN** and **5-PN** toward selected human cancer and normal cell lines

Polymer Nanoparticles	MCF-7		HepG2		Hep3B		Bel-7404		L02	
	24 h	48 h	24 h	48 h	24 h	48 h	24 h	48 h	24 h	48 h
2-PN ($\times 10^{-6}$ mol L^{-1})	94.22	34.74	70.71	62.65	77.49	28.40	25.71	10.03	102.21	55.64
5-PN ($\times 10^{-6}$ mol L^{-1})	114.51	46.97	103.77	81.91	177.44	84.02	42.92	19.78	115.23	39.79

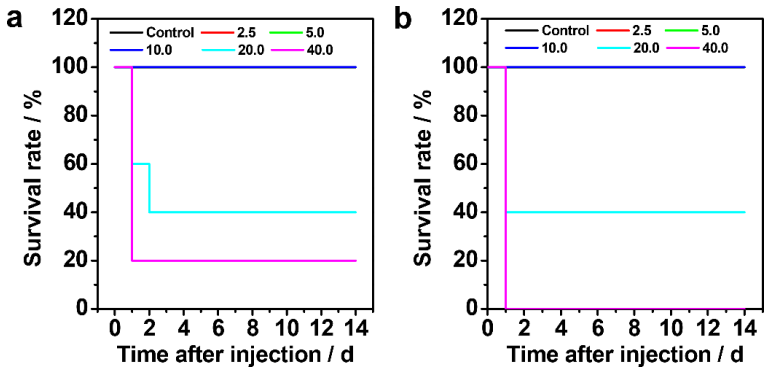

Fig. S60 Survival rate of mice in **2-PN** (a) and **5-PN** (b) groups (2.5, 5.0, 10.0, 20.0, and 40.0 mg/kg body weight).

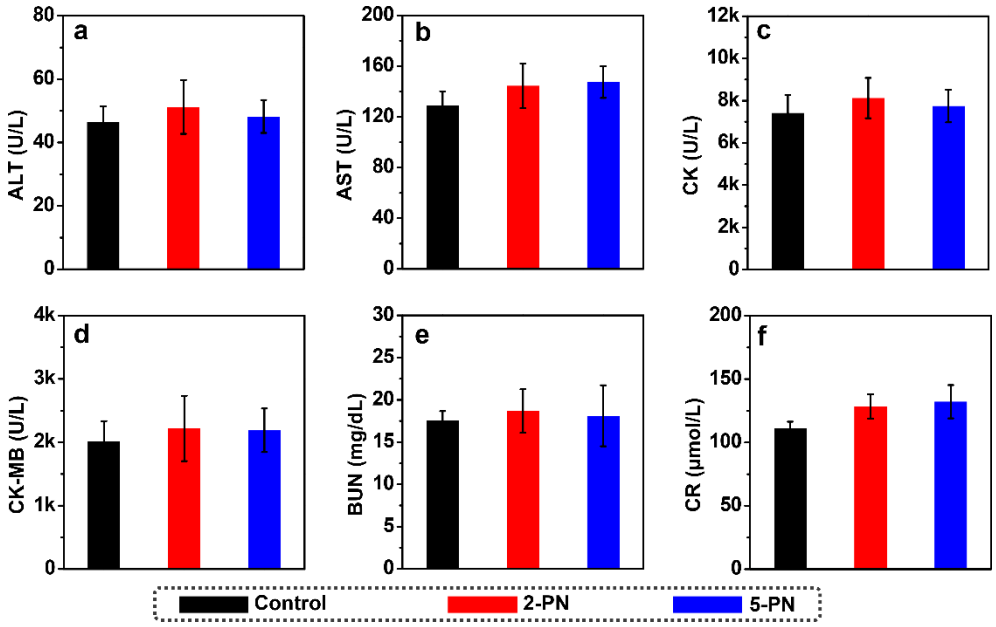

Fig. S61 Blood biochemical analysis of normal mice intravenously administered with PBS, **2-PN**, and **5-PN**. The terms are following: (a) alanine transaminase (ALT), (b) aspartate transaminase (AST), (c) creatine kinase (CK), (d) creatine kinase-MB (CK-MB), (e) blood urea nitrogen (BUN), and (f) creatinine (CR). Data are represented as mean ± SD.

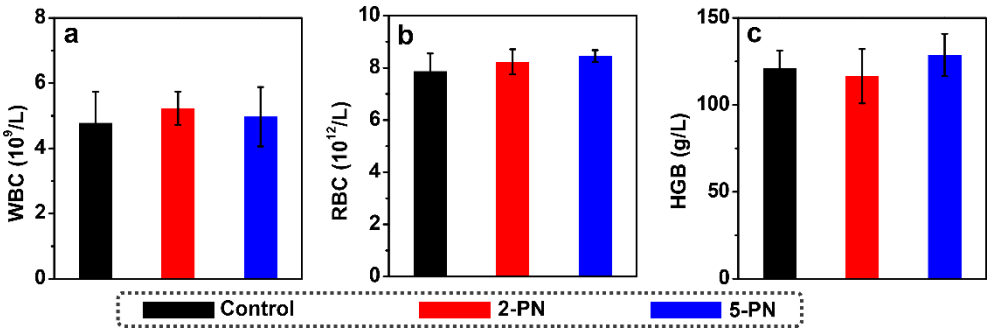

Fig. S62 Blood routine indexes of (a) white blood cell count (WBC), (b) red blood cell count (RBC), and (c) hemoglobin (HGB) of the healthy mice with the treatment of PBS, **2-PN**, or **5-PN**. Data are presented as mean ± SD.

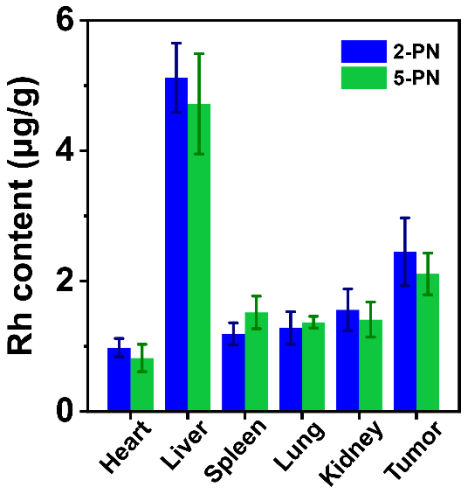

Fig. S63 ICP-MS analysis of the accumulation of Rh in major organs and tumors in Bel-7404-tumor-bearing nude mice intravenously administered with **2-PN** and **5-PN** at 72 h.

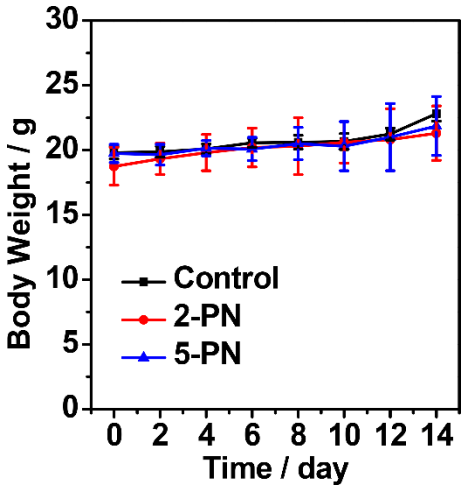

Fig. S64 Body weights of Bel-7404-tumor-bearing nude mice treated with PBS, **2-PN**, and **5-PN**.

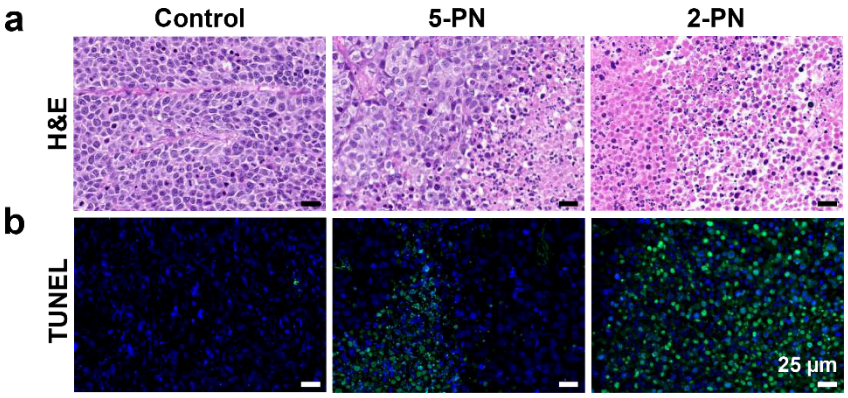

Fig. S65 (a) H&E staining and (b) immunofluorescence images of the tumor tissues.

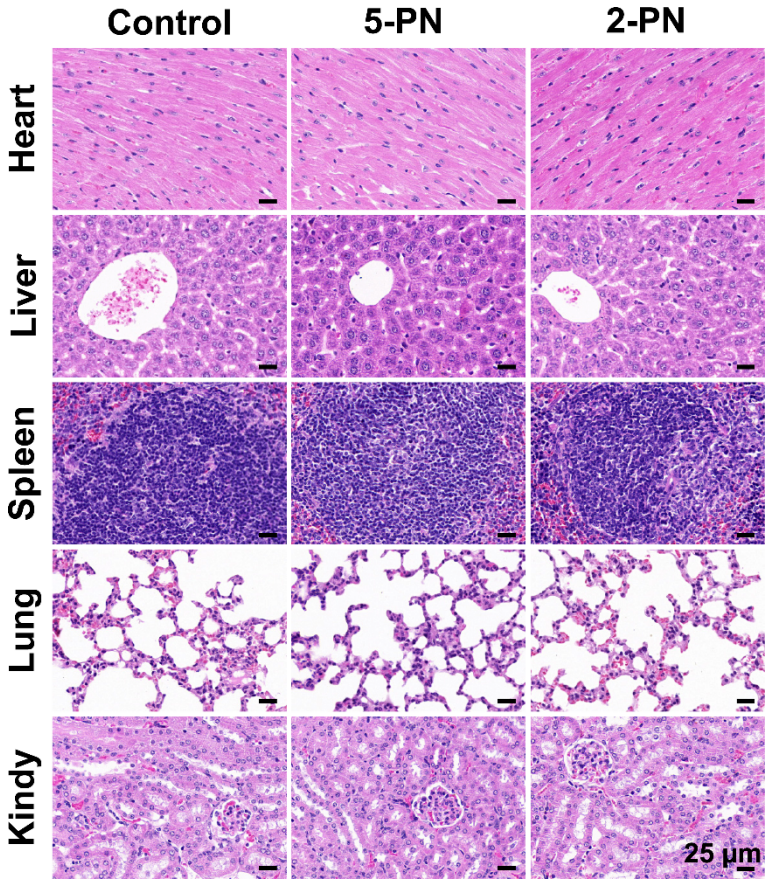

Fig. S66 H&E staining images of heart, liver, spleen, lung, and kidney of nude mice with PBS, **2-PN**, and **5-PN**.

3 Supporting References

[S1] X. Yan, S. Zhang, D. Peng, P. Zhang, J. Zhi, X. Wu, L. Wang, Y. Dong, X. Li, *Polym. Chem.* **2018**, *9*, 984−993.

[S2] a) K. Škoch, I. Císařová, P. Štěpnička, *Chem. Eur. J.* **2018**, *24*, 13788−13791; b) C. Wang, L. Wu, W. Xu, F. He, J. Qu, Y. Chen, *Org. Lett.* **2020**, *22*, 6954−6959.

[S3] C. Chu, J. A. Ayres, D. M. Stefanescu, B. R. Walker, C. B. Gorman, G. N. Parsons, *J. Phys. Chem. C* **2007**, *111*, 8080−8085.

[S4] a) M. Ishikawa, K. Maeda, Y. Mitsutsuji, E. Yashima, *J. Am. Chem. Soc.* **2004**, *126*, 732−733; b) Y. Hase, K. Nagai, H. Iida, K. Maeda, N. Ochi, K. Sawabe, K. Sakajiri, K. Okoshi, E. Yashima, *J. Am. Chem. Soc.* **2009**, *131*, 10719−10732; c) Y.-H. Wu, J. Zhang, F.-S. Du, Z.-C. Li, *ACS Macro Lett.* **2017**, *6*, 1398−1403.

[S5] a) I. Ugi, U. Fetzer, U. Eholzer, H. Knupfer, K. Offermann, *Angew. Chem., Int. Ed.* **1965**, *4*, 472−484; b) R. Obrecht, R. Herrmann, I. Ugi, *Synthesis* **1985**, *4*, 400−402.

[S6] X. Qiu, H. Xue, L. Xu, R. Wang, S. Qiu, Q. He, W. Bu, *Polym. Chem.* **2021**, *12*, 5191−5200.

[S7] J. Van Houten, R. J. Watts, *J. Am. Chem. Soc.* **1976**, *98*, 4853−4858.

[S8] Y. Yamamoto, K. Aoki, H. Yamazaki, *Inorg. Chem.* **1979**, *18*, 1681−1687.

[S9] K. R. Mann, N. S. Lewis, R. M. Williams, H. B. Gray, J. G. Gordon, *Inorg. Chem.* **1978**, *17*, 828−834.

[S10] A. K.-W. Chan, K. M.-C. Wong, V. W.-W. Yam, *J. Am. Chem. Soc.* **2015**, *137*, 6920−6931.

[S11] A. K.-W. Chan, D. Wu, K. M.-C. Wong, V. W.-W. Yam, *Inorg. Chem*. **2016**, *55*, 3685−3691.

[S12] A. K.-W. Chan, M. Ng, K.-H. Low, V. W.-W. Yam, *J. Am. Chem. Soc.* **2018**, *140*, 8321−8329.

[S13] Q. Wan, J. Xia, W. Lu, J. Yang, C.-M. Che, *J. Am. Chem. Soc.* **2019**, *141*, 11572−11582.

[S14] L. Li, N. Zhou, H. Kong, X. He, *Polym. Chem.* **2019**, *10*, 5465−5472.

[S15] J. A. Marsden, J. J. Miller, L. D. Shirtcliff, M. M. Haley, *J. Am. Chem. Soc.* **2005**, *127*, 2464−2476.

[S16] J.-S. Chen, R. B. Shirts, *J. Phys. Chem.* **1985**, *89*, 1643−1646.

[S17] N. Saito, R. Terakawa, M. Yamaguchi, *Chem. Eur. J.* **2014**, *20*, 5601−5607.

[S18] T. V. Jones, M. M. Slutsky, R. Laos, T. F. A. de Greef, G. N. Tew, *J. Am. Chem. Soc.* **2005**, *127*, 17235−17240.

[S19] P. A. Korevaar, C. Schaefer, T. F. A. de Greef, E. W. Meijer, *J. Am. Chem. Soc.* **2012**, *134*, 13482−13491.

[S20] J. Matern, K. K. Kartha, L. Sánchez, G. Fernández, *Chem. Sci.* **2020**, *11*, 6780−6788.

[S21] R. F. Goldstein, L. Stryer, *Biophys. J.* **1986**, *50*, 583−599.

[S22] K. H.-Y. Chan, H.-S. Chow, K. M.-C. Wong, M. C.-L. Yeung, V. W.-W. Yam, *Chem. Sci*. **2010**, *1*, 477−482.

[S23] M. H.-Y. Chan, S. Y.-L. Leung, V. W.-W. Yam, *J. Am. Chem. Soc.* **2019**, *141*, 12312−12321.

[S24] V. C.-H. Wong, C. Po, S. Y.-L. Leung, A. K.-W. Chan, S. Yang, B. Zhu, X. Cui, V. W.-W. Yam, *J. Am. Chem. Soc*. **2018**, *140*, 657−666.

[S25] S. Saita, Y. Mieno, Y. Kohno, H. Ohno, *Chem. Commun.* **2014**, *50*, 15450−15452.

[S26] Y. Mieno, Y. Kohno, S. Saita, H. Ohno, *Chem. Eur. J.* **2016**, *22*, 12262−12265.

[S27] E. M. Lewoczko, N. Wang, C. E. Lundberg, M. T. Kelly, E. W. Kent, T. Wu, M.-L. Chen, J.-H. Wang, B. Zhao, *ACS Appl. Polym. Mater.* **2021**, *3*, 867−878.